J. Fluid Mech. (1999), *vol.* 380, *pp.* 309–337. Printed in the United Kingdom

Minimal liquid bridges in non-axisymmetrically buckled elastic tubes

By MATTHIAS HEIL†

Department of Applied Mathematics and Theoretical Physics, University of Cambridge, Silver Street, Cambridge CB3 9EW, UK

(Received 20 February 1998 and in revised form 21 September 1998)

This study investigates the existence and stability of static liquid bridges in non-axisymmetrically buckled elastic tubes. The liquid bridge which occludes the tube is formed by two menisci which meet the tube wall at a given contact angle along a contact line whose position is initially unknown. Geometrically nonlinear shell theory is used to describe the deformation of the linearly elastic tube wall in response to an external pressure and to the loads due to the surface tension of the liquid bridge. This highly nonlinear problem is solved numerically by finite element methods.

It is found that for a large range of parameters (surface tension, contact angle and external pressure), the compressive forces generated by the liquid bridge are strong enough to hold the tube in a buckled configuration. Typical meniscus shapes in strongly collapsed tubes are shown and the stability of these configurations to quasi-steady perturbations is examined. The minimum volume of fluid required to form an occluding liquid bridge in an elastic tube is found to be substantially smaller than predicted by estimates based on previous axisymmetric models. Finally, the implications of the results for the physiological problem of airway closure are discussed.

1. Introduction

The lung's airways are coated with a thin liquid film which affects many aspects of its mechanical behaviour (Grotberg 1994; West 1995). In the smaller airways, where the wall curvature is large, the surface tension of the liquid film is important and is generally believed to be the cause of 'airway closure' which has been observed directly (Macklem, Proctor & Hogg 1970) and indirectly (Otis *et al.* 1996) in the excised lungs of laboratory animals. Airway closure occurs through the formation of liquid bridges which occlude the airway lumen. The formation of these liquid bridges is assumed to follow the growth of a Rayleigh instability of the liquid lining which Kamm & Schroter (1989) refer to as 'film collapse'. The formation of the liquid bridge can be accompanied (and indeed dominated) by large elastic deformations of the airway walls, leading to a so-called 'compliant collapse'.

Many important contributions to the understanding of this problem have been made over the past three decades: Everett & Haynes (1972) and Kamm & Schroter (1989) carried out experimental investigations into the formation of liquid bridges in rigid circular tubes and established the minimum volume of liquid required to form an occluding liquid bridge. Goren (1962), Hammond (1983), Gauglitz & Radke (1988)

† Present Address: Department of Mathematics, University of Manchester, Oxford Road, Manchester M13 9PL. E-mail: M.Heil@maths.man.ac.uk.

and Johnson *et al.* (1991) studied the evolution of disturbances to an annular liquid film inside a rigid tube after the film has undergone a Rayleigh instability. Halpern & Grotberg (1992, 1993) investigated how wall elasticity affects the formation of the liquid bridge and derived coupled evolution equations for the film thickness and wall deformation in a thin-walled axisymmetric elastic tube. By following the evolution of the air–liquid interface until its minimum radius approached zero at some point along the tube, it was shown that occluding liquid bridges do indeed form for a wide range of parameter values. The computations were usually stopped shortly before the minimum radius was reduced to zero and hence before the liquid bridge was actually formed. Following the formation of a liquid bridge, fluid will continue to drain from the liquid lining into the liquid bridge until the film ruptures or until (asymptotically) the film thickness has been reduced to zero. For an axisymmetric tube, the final steady state of the combined fluid–elastic instability is an axisymmetric liquid bridge formed by two spherical air–liquid interfaces which meet the (possibly deformed) tube wall at a constant contact angle γ. During the draining of the liquid film, satellite liquid collars, which become disconnected from the main liquid bridge, can develop (see e.g. Gauglitz & Radke 1988).

Throughout the formation of the liquid bridge, the pressure exerted by the fluid on the tube wall is most compressive in the region where the liquid bridge is being formed. Given the rather large axisymmetric deflections of up to 20% of the tube's radius (Halpern & Grotberg 1992, 1993), the question arises of whether the tube wall will indeed remain axisymmetric. Typically, thin-walled cylindrical tubes buckle when their axisymmetric pre-buckling deformations are much smaller. In this context, it is interesting to note that most investigations of airway re-opening (i.e. the reversal of the process discussed above) assume that the occluded airway is indeed in a strongly collapsed state such that the flattened opposite walls of the airway have to be 'peeled apart' during the re-opening (e.g. Gaver, Samsel & Solway 1990).

Ultimately, this question will need to be studied by examining the stability of the time-dependent axisymmetric wall and air–liquid interface shapes to non-axisymmetric disturbances. The investigation of the system's evolution to a final steady state (in which a liquid bridge might or might not have formed in the buckled tube) would require the solution of a large-displacement fluid–structure interaction problem with two free surfaces. An alternative (and computationally much cheaper) approach is pursued in this paper which examines the existence and stability of static liquid bridges in axisymmetric and non-axisymmetrically buckled elastic tubes. We investigate under what circumstances the compressive forces exerted by a liquid bridge on the wall of a long thin-walled tube of initially circular cross-section are large enough to keep the tube wall in a buckled shape. This will establish the necessary criteria for the existence of stable liquid bridges in non-axisymmetrically buckled tubes and will also allow us to determine the minimum volume of fluid required to form an occluding liquid bridge in an elastic tube.

The paper is organized as follows. In § 2 we will introduce the model problem considered in this study and discuss the variational equations governing the wall deformation and the meniscus shapes. Sections 2.3 and 2.4 discuss the interaction between the liquid bridge and the tube wall and the choice of parameters and boundary conditions to be used for the study. Section 3 presents the procedure employed for the numerical solution of the coupled fluid–structure interaction problem. The results are presented in § 4: first we consider the shapes of menisci in uniformly buckled tubes (corresponding to the limiting case when the air–liquid surface tension is very small and the pressure jump over the menisci can be neglected). This subsection helps to

explain some of the results presented in § 4.2, which is concerned with minimal liquid bridges in non-uniformly buckled tubes. Section 4.3 investigates the stability of the liquid bridges to quasi-steady perturbations. Finally, § 5 examines the relevance of the findings to the airway closure problem.

2. The model

We will investigate a conceptually simple model problem which focuses on the interaction of the liquid bridge with the non-axisymmetric deformation of the elastic tube in which it is contained. The tube will be modelled as a thin-walled, linearly elastic shell which is partly filled with fluid. The tube deforms in response to an external pressure p^*_{ext} and to the additional loads induced by the surface tension σ^* of the air–liquid interfaces. For simplicity we will neglect gravitational effects. Under these conditions, the two menisci enclosing the liquid bridge are surfaces of constant mean curvature which meet the tube wall at a prescribed contact angle γ along two contact lines whose position has to be determined as part of the solution.

2.1. *The shell equations*

We use a geometrically nonlinear Kirchhoff–Love-type shell theory (described in detail in Heil & Pedley 1996 and Heil 1997) to model the deformation of the cylindrical tube of midplane radius R_0 and wall thickness h. We express the tube's deformation in terms of the dimensionless midplane displacements $\boldsymbol{v} = \boldsymbol{v}^*/R_0$. The superscript star distinguishes dimensional quantities from their non-dimensional equivalents. We use Lagrangian coordinates $\xi^\alpha = \xi^{*\alpha}/R_0$ (Greek and italic indices have values 1, 2 and 1, 2, 3, respectively, and the summation convention is used) to parametrize the shell's midplane such that the non-dimensional vector from the origin of a spatially fixed Cartesian coordinate system, (x, y, z), to the undeformed midplane, $\boldsymbol{r}^0 = \boldsymbol{r}^{*0}/R_0$, is given by

$$\boldsymbol{r}^0 = \left(\sin(\xi^2), \cos(\xi^2), \xi^1\right)^T, \quad \xi^2 \in [0, 2\pi]. \tag{1}$$

The parametrization of the tube is illustrated in figure 1. The position of a material point at a non-dimensional distance $\xi^3 = \xi^{*3}/R_0$ from the shell's undeformed midplane is then given by

$$\boldsymbol{r} = \boldsymbol{r}^0 + \xi^3 \boldsymbol{n}_w, \quad \xi^3 \in [-h/(2R_0), h/(2R_0)], \tag{2}$$

where $\boldsymbol{n}_w = \left(\sin(\xi^2), \cos(\xi^2), 0\right)^T$ is the outward normal vector on the undeformed midplane.

After the deformation, the material point on the midplane with the Lagrangian coordinates ξ^α has been displaced to a new position $\boldsymbol{R}^0(\xi^\alpha) = \boldsymbol{r}^0(\xi^\alpha) + \boldsymbol{v}(\xi^\alpha)$. We decompose the displacement vector $\boldsymbol{v}$ into the undeformed basis, $\boldsymbol{v} = v^j \, \boldsymbol{a}_j$, where the undeformed base vectors are given by $\boldsymbol{a}_\alpha = \boldsymbol{r}^0_{,\alpha}$ and $\boldsymbol{a}_3 = \boldsymbol{n}_w$. The comma denotes the partial derivative with respect to the Lagrangian coordinates. Lowercase and uppercase letters are used for shell variables associated with the undeformed and deformed geometry, respectively.

The Kirchhoff–Love assumption states that material lines which were normal to the undeformed midplane remain normal to the shell's midplane thoughout its deformation and that they remain unstretched. Therefore, the vector to an arbitrary material point in the shell after the deformation is given by

$$\boldsymbol{R} = \boldsymbol{R}^0 + \xi^3 \boldsymbol{N}_w, \tag{3}$$

where $\boldsymbol{N}_w$ is the outward normal vector on the deformed shell.

It has been shown previously (e.g. Heil & Pedley 1996) that even though the buckling tube undergoes large displacements, the wall's extensional deformation remains small. This allows the use of Hooke's law as the constitutive equation. Then the principle of virtual displacements which governs the shell's deformation is given by (see Wempner 1973)

$$\int\int \left[E^{\alpha\beta\gamma\delta} \left(\gamma_{\alpha\beta}\ \delta\gamma_{\gamma\delta} + \frac{1}{12}\left(\frac{h}{R_0}\right)^2 \kappa_{\alpha\beta}\ \delta\kappa_{\gamma\delta} \right) - \frac{1}{12(1-\nu^2)}\left(\frac{h}{R_0}\right)^2 (\boldsymbol{f}\cdot\delta\boldsymbol{R})\,|_{\xi^3=\pm h/(2R_0)} \right] \mathrm{d}\xi^1\,\mathrm{d}\xi^2 - \int_S \frac{1}{12(1-\nu^2)}\left(\frac{h}{R_0}\right)^2 (\boldsymbol{l}\cdot\delta\boldsymbol{R})\,|_{\xi^3=-h/(2\boldsymbol{R}_0)} \mathrm{d}s = 0, \quad (4)$$

where $\boldsymbol{f} = \boldsymbol{f}^*/K$ is the traction per unit area of the undeformed midplane, non-dimensionalized with the tube's bending stiffness $K = E(h/R_0)^3/[12(1-\nu^2)]$ and $\boldsymbol{l}$ represents a line force (a force per unit length acting along the line S on the inside of the tube – this will be made more specific below). $\gamma_{\alpha\beta}$ and $\kappa_{\alpha\beta}$ are the non-dimensional strain and bending tensors, respectively, and the dimensionless plane stress stiffness tensor, $E^{\alpha\beta\gamma\delta} = E^{*\alpha\beta\gamma\delta}/E$ is given by

$$E^{\alpha\beta\gamma\delta} = \frac{1}{2(1+\nu)}\left(\delta^{\alpha\gamma}\delta^{\beta\delta} + \delta^{\alpha\delta}\delta^{\beta\gamma} + \frac{2\nu}{1-\nu}\delta^{\alpha\beta}\delta^{\gamma\delta}\right), \quad (5)$$

where the tube's Poisson ratio and its elastic modulus are denoted by ν and E, respectively. The variations of strain and bending tensors have to be taken with respect to the displacements v^i and their derivatives.

2.2. *The meniscus equations*

Using the Lagrangian coordinates ξ^α introduced in the previous section, the vector to a material point on the inside of the tube wall is given by $\boldsymbol{R}_w(\xi^\alpha) = \boldsymbol{R}(\xi^\alpha, \xi^3 = -h/(2R_0))$. We will assume that the contact line can be parametrized in the form $\xi^1 = \xi_c^1(\xi^2)$; see figure 1.

For small contact angles and large wall slopes, parts of the meniscus might not project simply onto the (x, y)-plane (see figure 2). Therefore, the meniscus shape needs to be determined in parametric form: we choose a set of surface coordinates ζ_α (where $\zeta_1^2 + \zeta_2^2 \leqslant 1$) to parametrize the meniscus such that the meniscus shape is given by $\boldsymbol{R}_m(\zeta_1, \zeta_2)$ and the contact line is parametrized by $\varphi = \arctan(\zeta_1/\zeta_2)$ as

$$\boldsymbol{R}_c(\varphi) = \boldsymbol{R}_m(\sin(\varphi), \cos(\varphi)), \quad \varphi \in [0, 2\pi]. \quad (6)$$

To ensure that the meniscus boundary coincides with the contact line on the wall, parametrized by $\xi_c^1(\xi^2)$, we choose the meniscus parametrization such that $\varphi = \xi^2$ and thus obtain

$$\boldsymbol{R}_c(\varphi) = \boldsymbol{R}_w(\xi_c^1(\varphi), \varphi). \quad (7)$$

The contact angle γ is given by

$$\gamma = \mathrm{sgn}(\boldsymbol{T}\cdot\boldsymbol{N}_w)\arccos(\boldsymbol{N}_m\cdot\boldsymbol{N}_w), \quad (8)$$

where $\boldsymbol{N}_m = (\boldsymbol{R}_{m,1}\times\boldsymbol{R}_{m,2})/|\boldsymbol{R}_{m,1}\times\boldsymbol{R}_{m,2}|$ is the normal vector on the meniscus and $\boldsymbol{T} = (\boldsymbol{N}_m\times\boldsymbol{R}_{c,\varphi})/|\boldsymbol{N}_m\times\boldsymbol{R}_{c,\varphi}|$ is the vector tangential to the meniscus and normal to the contact line.

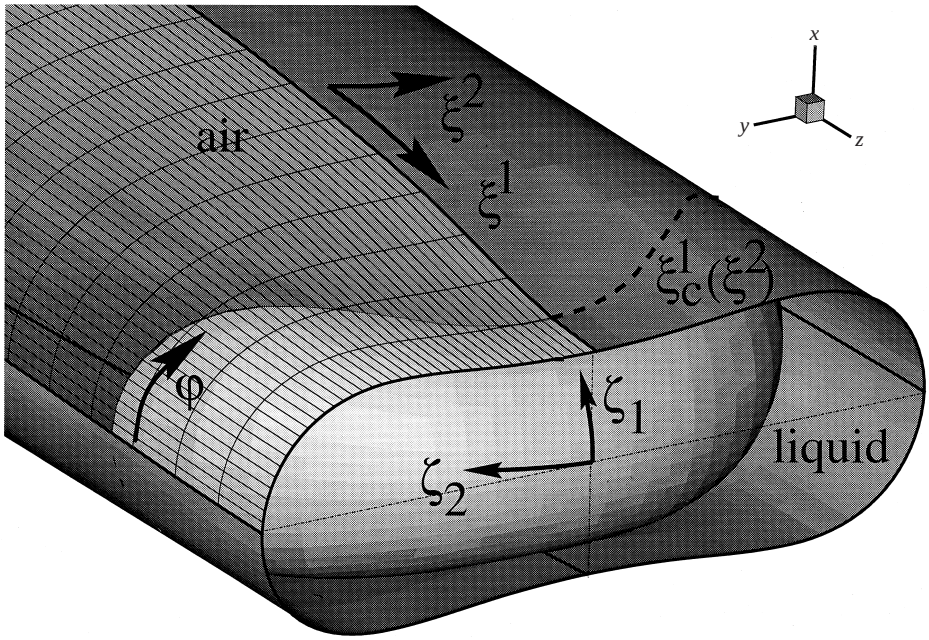

FIGURE 1. Sketch of the buckled tube containing a meniscus. The ξ^α and ζ_α coordinates parametrize the tube wall and the meniscus, respectively. $\xi^1 = \xi^1_c(\xi^2)$ and $\varphi = \arctan(\zeta_1/\zeta_2)$ are used to parametrize the contact line in the shell and meniscus coordinates, respectively.

The meniscus shape is determined by the principle of virtual displacements (Landau & Lifshitz 1987),

$$\int\!\!\int \left(\delta \mathscr{A}_m^{1/2} - \kappa\, \boldsymbol{N}_m \cdot \delta \boldsymbol{R}_m \mathscr{A}_m^{1/2}\right) \mathrm{d}\zeta_1\, \mathrm{d}\zeta_2 = 0, \tag{9}$$

which equates the work done by the non-dimensional pressure jump, $\Delta p = \Delta p^*/K$, over the meniscus during a virtual displacement of the meniscus, with the change in the meniscus' non-dimensional surface energy, $\sigma \mathscr{A}_m^{1/2}$. The non-dimensional surface tension, $\sigma = \sigma^*/(R_0 K)$ represents the ratio of the typical pressure jump over the air–liquid interfaces to the tube's bending stiffness and $\mathscr{A}_m = |\boldsymbol{R}_{m,1} \times \boldsymbol{R}_{m,2}|^2$ is the determinant of the metric tensor of the surface parametrized by (ζ_1, ζ_2). Only the parameter κ which is equal to twice the mean curvature of the interface appears in the variational equation since the pressure jump over the interface is related to the surface tension by $\Delta p = \sigma\kappa$.

The variational equation (9) has to be augmented by various boundary conditions. First, either the contact line position $\xi^1_c(\varphi)$ or the contact angle $\gamma(\varphi)$ have to be prescribed. Second, we need to prescribe the volume of fluid, $\mathscr{V}$, contained in the liquid bridge or apply a displacement constraint which directly prescribes the axial position of one point on the meniscus, e.g. $\boldsymbol{R}_m(0,0) = (0,0,\hat{Z})^T$. The meniscus curvature, κ, plays the role of a Lagrange multiplier for the volume or displacement constraint and has to be determined as part of the solution.

2.3. *The meniscus–wall interaction*

Three different surface tensions, σ_{wl}, σ_{wa} and σ, act at the three material interfaces (wall–liquid, wall–air and air–liquid, respectively). Since the system is at rest, the bulk

fluid pressures in the air-filled and liquid-filled parts of the tube are constant. The pressure jump over the three interfaces is given by the products of their curvature with the respective surface tensions (see e.g. Batchelor 1967). We neglect the effect of the so-called 'line tension' (a tension acting along the contact line, apparently first discussed by Gibbs 1906) since its influence on the macroscopic behaviour of the three material interfaces is believed to be negligible (see e.g. Pethica 1977).

We set the reference pressure in the air-filled part of the tube to $p_{air} = 0$. Then the non-dimensional bulk pressure in the liquid-filled part of the tube is given by $p_{liquid} = -\sigma\kappa$, where κ is the constant curvature of the air–liquid interface.

The equilibrium of forces at the contact line in the direction tangential to the wall establishes Young's equation for the contact angle,

$$\cos\gamma = \frac{\sigma_{wa} - \sigma_{wl}}{\sigma}, \tag{10}$$

and the equilibrium in the direction normal to the wall shows that the normal component of the air–liquid surface tension acts as a line force on the tube wall. The presence of this line force was investigated by various authors who studied the deformation of thin (visco-)elastic sheets onto which small drops of high-surface-tension liquids were deposited (see e.g. Fortes 1984; Shanahan 1985; Carré, Gastel & Shanahan 1996; Extrand & Kumagai 1996 and Long, Ajdari & Leibler 1996). It should be noted that, similarly to the pressure jump over the air–liquid interface, the wall–liquid and wall–air surface tensions make the normal stress experienced by the curved tube wall different from the bulk pressures in the respective fluids. This effect is negligible for surfaces of zero initial curvature, such as those considered in the above-mentioned experimental studies on plane elastic sheets. However, for the geometry considered here, it is not immediately obvious if the pressure jumps across the fluid–wall interfaces have a significant effect on the wall deformation: Consider the case of an air–liquid interface which meets the undeformed axisymmetric tube of radius R at a small contact angle. In this case the pressure jump over the meniscus is approximately $\Delta p \approx 2\sigma/R$ and we have implicitly assumed that this pressure jump is large enough to lead to a significant bending deformation of the tube wall. Now equation (10) shows that for small contact angles the two fluid–wall surface tensions σ_{wa} and σ_{wl} have to be of the same order of magnitude as (or even larger than) the air–liquid surface tension σ. This is also confirmed by experimental measurements of these quantities (see e.g. Bailey 1961 and Bailey & Kay 1967). Given that the wall curvature, $\kappa_w = 1/R$, is of the same order of magnitude as the meniscus curvature, this indicates that the pressure jump over the fluid–wall interfaces is comparable with the pressure jump over the meniscus and hence important. This observation leads to the surprising implication that the mere submersion of a sufficiently thin cylindrical tube in a liquid should lead to a noticeable deformation (note that the wall–fluid surface tensions on the inside and on the outside of the tube wall act in the same sense). This does not seem to have been observed experimentally.

The apparent paradox is resolved by realizing that a positive surface tension attempts to minimize the interfacial area. In the case of the fluid–wall surface tensions, this can only be achieved by compressing the tube wall in-plane. Since the tube's extensional stiffness is much larger than its bending stiffness, the corresponding deformation is much smaller than the deformation due to the pressure jump over the air–liquid interface which has to be balanced by the tube's bending stiffness when the tube is in its buckled state.

Consequently, we neglect the effect of the fluid–wall surface tensions and thus

obtain the traction $\boldsymbol{f}$ on the wall as

$$\boldsymbol{f} = \begin{cases} -p_{ext}\boldsymbol{N}_w & \text{for } \xi^1 < \xi_c^1(\xi^2) \\ (-p_{ext} - \sigma\kappa)\boldsymbol{N}_w & \text{for } \xi^1 \geqslant \xi_c^1(\xi^2). \end{cases} \tag{11}$$

The line force $\boldsymbol{l}$ in the variational equation (4) is given by the normal component of the surface tension along the contact line, $\sigma \boldsymbol{T} \cdot \boldsymbol{N}_w$, therefore we have

$$\int_S (\boldsymbol{l} \cdot \delta \boldsymbol{R})\,|_{\xi^3 = -h/(2\boldsymbol{R}_0)}\, \mathrm{d}s = \int_0^{2\pi} ((\sigma \boldsymbol{T} \cdot \boldsymbol{N}_w)\boldsymbol{N}_w \cdot \delta \boldsymbol{R}_w) \left| \frac{\partial \boldsymbol{R}_c(\varphi)}{\partial \varphi} \right| \mathrm{d}\varphi. \tag{12}$$

2.4. *Choice of parameters and boundary conditions*

So far we have not specified the boundary conditions to be applied to the shell equations. Most previous theoretical investigations were concerned with infinitely long tubes whose deformation was assumed to be periodic in the axial direction. The axial wavelength of the periodic deformation was assumed to be that of the most strongly growing mode obtained from the linear stability analysis. This was shown to depend on, amongst other parameters, the wall damping (Halpern & Grotberg 1992) which does not play a direct role in the present investigation since only steady states are considered.

We will enforce axially periodic deformations of the tube but impose the symmetry conditions far away from the meniscus in order to minimize their direct effect on the tube's interaction with the liquid bridge. We choose a wall thickness of $h/R = 1/20$ which is close to the limits of the applicability of thin-shell theory and set Poisson's ratio to $v = 0.49$ to model the near incompressible behaviour of biological tissue or rubber – the latter being the more likely material to be used in a laboratory experiment.

The boundary conditions for the meniscus depend on the particular problem under consideration and will be discussed where appropriate.

3. The numerical solution

The numerical solution of the shell equations, with the load terms specified by (11) and (12), was achieved by discretizing the variational equation (4) with N_w quadrilateral Hermite finite elements (Bogner, Fox & Schmit, 1967). This followed the approach taken in Heil & Pedley (1996) where more details of the implementation and validation can be found. The solution of the variational equation (9) for the meniscus shape is problematic since the variational equation only determines the meniscus shape but not its parametrization. Infinitely many two-parameter vector functions $\boldsymbol{R}_m(\zeta_\alpha)$ parametrize the same meniscus shape (this is an important difference to the Lagrangian description of the tube wall, in which the coordinates ξ^α label material points). The corresponding lack of compactness is usually overcome by the imposition of additional constraints on the parametrization, e.g. by requiring that the mapping from the ζ_α-unit disk to the meniscus be conformal (see e.g. Struwe 1988). A computationally more efficient approach is given by the method of spines (e.g. Kistler & Scriven 1983 and Rast 1994) which we will employ here. We will only allow the points on the meniscus to move along certain predetermined vectors, $\boldsymbol{S}(\zeta_1, \zeta_2)$, (the spines) in space. The spines have to be chosen in advance such that each point on the meniscus is only intersected by one spine. Then only a scalar field, $w(\zeta_1, \zeta_2)$, which represents the displacement along the spines needs to be determined.

For the present problem, the spines need to be chosen such that: (i) the boundary

of the meniscus meets the wall along the contact line and (ii) meniscus shapes which do not project simply onto the (x, y)-plane can be represented. This is achieved by splitting the position vector to the meniscus into two components

$$\boldsymbol{R}_m(\zeta_1, \zeta_2) = \boldsymbol{B}(\zeta_1, \zeta_2) + w(\zeta_1, \zeta_2)\, \boldsymbol{S}(\zeta_1, \zeta_2). \tag{13}$$

To fulfil condition (i) we choose the vector to the spine origin, $\boldsymbol{B}(\zeta_1, \zeta_2)$, such that $\boldsymbol{B}(\sin(\varphi), \cos(\varphi)) = \boldsymbol{R}_c(\varphi)$ and require that the scalar displacement field, w, vanishes at the boundary, i.e. $w(\sin(\varphi), \cos(\varphi)) = 0$. A simple choice for $\boldsymbol{B}(\zeta_1, \zeta_2)$ which works well for moderately collapsed tubes and illustrates the general idea is

$$B^\alpha(\zeta_1, \zeta_2) = \rho R_c^\alpha(\varphi), \tag{14}$$

$$B^3(\zeta_1, \zeta_2) = R_c^3(\varphi) + (1 - \rho)(\hat{R}_c^3 - R_c^3(\varphi)), \tag{15}$$

where $\varphi = \arctan(\zeta_1/\zeta_2)$, $\rho = (\zeta_1^2 + \zeta_2^2)^{1/2}$ and $\hat{R}_c^3$ is an arbitrary constant which was set to $\hat{R}_c^3 = \max_\varphi R_c^3(\varphi)$. A better choice which was used for the computations in strongly collapsed tubes is given in Appendix A. To fulfil condition (ii) the spines must be inclined away from the tube's axis near the contact line while symmetry requires them to be parallel to the tube's axis on the centreline. A simple choice which proved sufficient for all computations is given by

$$S^\alpha(\zeta_1, \zeta_2) = \frac{\rho \zeta_\alpha}{\bar{R}} \left[\frac{\rho^4}{\bar{R}^2} + \left(1 - \left(\frac{\rho}{\bar{R}}\right)^2\right)^2 \right]^{-1/2}, \tag{16}$$

$$S^3(\zeta_1, \zeta_2) = \left(1 - \left(\frac{\rho}{\bar{R}}\right)^2\right) \left[\frac{\rho^4}{\bar{R}^2} + \left(1 - \left(\frac{\rho}{\bar{R}}\right)^2\right)^2 \right]^{-1/2}. \tag{17}$$

The required change in the spines' orientation is achieved by the terms outside the square brackets (the terms in the square brackets merely normalize the spines to unit length). On the tube's centreline the spines point in the axial direction, $\boldsymbol{S}(0, 0) = \boldsymbol{e}_z$; the parameter $\bar{R}$ controls the extent to which the spines rotate outwards as one approaches the contact line ($\rho = 1$): $\bar{R} \to 1$ makes them point radially outwards on the contact line; for $\bar{R} \to \infty$ they remain parallel to the z-axis. For most computations a value in the range between $\bar{R} = 5$ and $\bar{R} = 10$ was used. The spines are illustrated in figure 2.

We insert (13) into (9), carry out the variations with respect to the displacement field w and its derivatives with respect to the surface coordinates ζ_α and thus transform (9) into

$$\int\int \left(\frac{\partial \mathscr{A}_w^{1/2}}{\partial w} \delta w + \frac{\partial \mathscr{A}_w^{1/2}}{\partial w_{,\alpha}} \delta w_{,\alpha} - \kappa\, \boldsymbol{N}_w \cdot \boldsymbol{S}\, \mathscr{A}_w^{1/2}\, \delta w \right) \mathrm{d}\zeta_1 \mathrm{d}\zeta_2. \tag{18}$$

To discretize this equation we decompose the ζ_α-domain into N_m isoparametric finite elements and express the displacement field $w(\zeta_\alpha)$ as

$$w = \sum_j W^j \psi_j, \tag{19}$$

where the ψ_j are two-dimensional piecewise quadratic shape functions (see e.g. Becker, Carey & Oden 1984). After substituting (19) into (18) we carry out the variations with respect to the discrete displacements, W^j, and obtain M_m equations for those $W^j (j = 1, M_m)$ which are not determined by the boundary conditions. The displacement (or volume) constraint provides the additional equation required for the

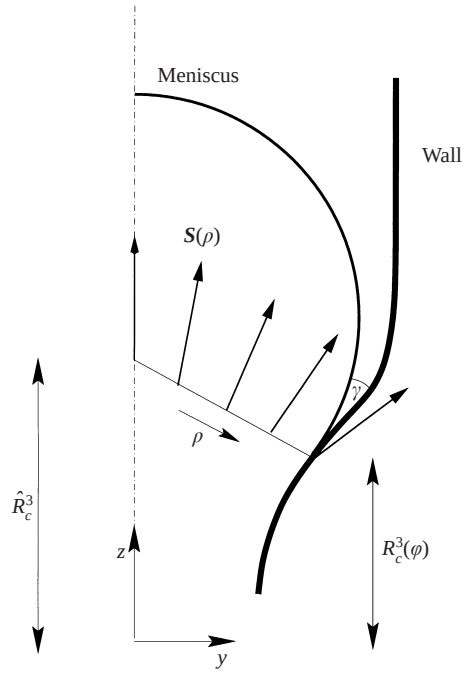

FIGURE 2. Sketch illustrating the representation of the meniscus using spines. The points on the meniscus are only allowed to move in the direction of the spines $\boldsymbol{S}$. The spines rotate outwards as they approach the contact line, thus allowing the representation of menisci which do not project simply into the (x, y)-plane. The origins of the spines are coupled to the contact line position.

determination of the meniscus curvature κ. If the contact line position is prescribed then these M_m+1 equations completely determine the meniscus shape and the contact angle can be obtained from (8).

In order to enforce a constant contact angle, we have to allow the contact line to move. For this purpose we discretize the contact line parametrization, $\xi_c^1(\varphi)$, with N_c one-dimensional isoparametric finite elements such that

$$\xi_c^1 = \sum_j X^j \hat{\psi}_j, \tag{20}$$

where the $\hat{\psi}_j$ are one-dimensional piecewise quadratic shape functions. The additional equations required to determine the unknown contact line parameters $X^j (j = 1, M_c)$ were determined by a Galerkin method in which the residual of the contact angle equation, $\gamma(\varphi) - \gamma_{prescribed} = 0$, was weighted with the shape functions $\hat{\psi}_j$.

An automatic mesh generator (described in detail in Heil 1998) was used to generate a three dimensional volume mesh for the determination of the volume of fluid contained in the liquid bridge. The symmetry of the buckled configuration requires the discretization of only a quarter of the respective domains ($\xi^2 \in [0, \pi/2], \zeta_\alpha \geqslant 0$) and the application of appropriate symmetry boundary conditions. The highly nonlinear coupled system of equations was solved with a Newton–Raphson method which was embedded in an adaptive continuation procedure. This procedure allowed the computation of solutions which correspond to menisci in strongly collapsed tubes through a sequence of intermediate states, starting with a slightly buckled tube for which the undeformed axisymmetric configuration provided a good initial guess.

In order to validate the newly developed meniscus solver, a wall shape with elliptical cross-sections whose major and minor axes varied linearly with ξ^1 as $\boldsymbol{R}_w = [(a_0+(a_1-a_0)\xi^1)\cos(\xi^2), (b_0+(b_1-b_0)\xi^1)\sin(\xi^2), \xi^1]^T$ was chosen. The intersection of this wall with a sphere of radius $2/\kappa$, with centre-point at the origin, was determined analytically and the variable contact angle along the contact line was prescribed as the input for the numerical computation. The parameters were chosen such that the contact line extended across the sphere's equator ($a_0 = 1.4, a_1 = b_1 = 2.3, b_0 = 1.7, \kappa = 1.351$) thus creating a meniscus which did not project simply onto the (x, y)-plane. For $N_m = 52$ internal elements and $N_c = 8$ elements for the contact line (a total of 252 degrees of freedom), the relative r.m.s.-errors for the meniscus shape and the contact line position were 2.31×10^{-6} and 7.0×10^{-4}, respectively. This test was repeated for a range of parameters and similar results were obtained. Further test cases in axially uniform tubes included Concus & Finn's (1974) spherical cap in a cylinder of quadratic cross-section and the intersection of Scherk's surface (a surface of zero mean-curvature; see e.g. Carmo 1976) with an elliptical cylinder. A consistency test for the computed values of the contact line position and the meniscus curvature was carried out using equation (B 4) which is derived in Appendix B.

In most computations presented below, the wall, the meniscus and the contact line were discretized with $N_w = 66, N_m = 52$ and $N_c = 8$ finite elements resulting in a total of 1053 degrees of freedom. The mesh independence of the numerical results was confirmed by repeating selected computations with an increased resolution. An example of this is shown in figure 6 below, in which the solid line shows the results obtained from a computation with the standard resolution while the dotted line shows the results obtained with a finer resolution using $N_w = 120, N_m = 116$ and $N_c = 12$ elements (1977 degrees of freedom).

The most expensive part of the computation is the setup of the global Jacobian matrix and the solution of the linear systems (using LU-decomposition) during the Newton–Raphson iteration. A typical computation, tracing the tube's deformation and the corresponding meniscus shape from a slightly buckled to a strongly collapsed configuration required several hours of CPU time on a DEC Alpha workstation.

4. Results

4.1. *Menisci in uniformly collapsed tubes;* $\sigma = 0$

We will first examine the case in which the non-dimensional surface tension σ is zero so that the pressure jump over the meniscus does not affect the tube's deformation which is therefore controlled by the external pressure alone. In this case the tube deforms uniformly (i.e. without any axial variations) and it buckles non-axisymmetrically when the external pressure exceeds the buckling pressure $p_{ext}^{(crit)} = 3$ (see e.g. Simitses 1976). For small and moderately large buckling deformations, the tube's cross-sectional area is approximately elliptical; for larger deformations it becomes dumb-bell shaped. This is illustrated in figure 3 which shows a sequence of increasingly collapsed tubes containing a single meniscus. Since the tube's deformation is uniform, the axial position of the meniscus is arbitrary and was chosen such that the apex of the meniscus remained at the 'end' of the tube at $z = 0$, i.e. $\max R_m^3 = z_{m(max)} = 0$. The tube's deformation characteristics are illustrated in figure 4 (*a*) where the solid line shows the relation between the external pressure, p_{ext}, and the tube's non-axisymmetric deformation, characterized by the radial wall displacement v_{ctrl} at the most strongly collapsed point in the tube (in the plane $y = 0$). The plot shows that an increase in

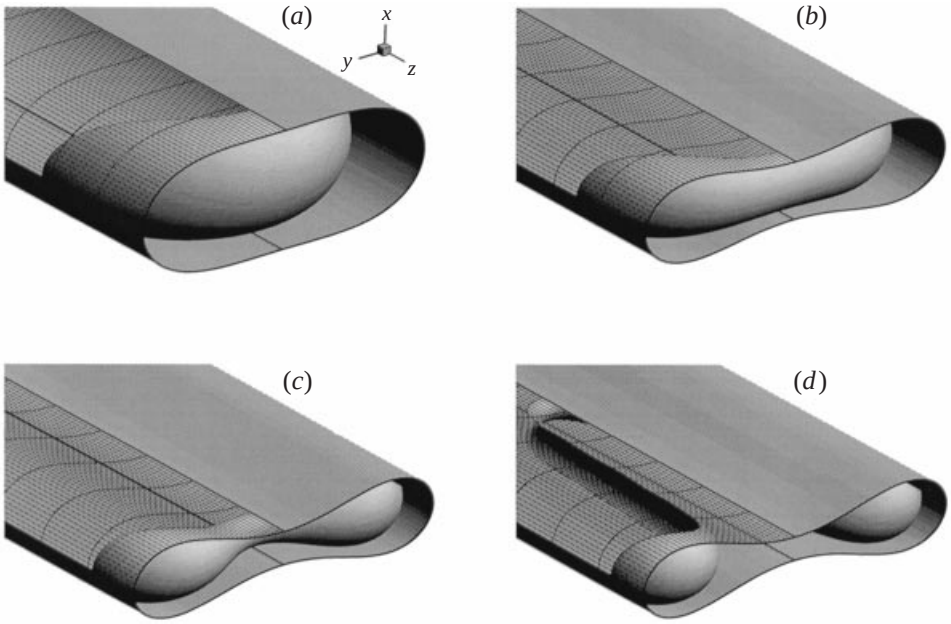

FIGURE 3. Sequence of uniformly collapsed tubes containing a single meniscus. As the tube's collapse increases, the meniscus develops a long finger along the tube's centreline. The contact angle is $\gamma = 10^\circ$. (*a*) $v_{ctrl} = -0.450$, $p_{ext} = 3.41$; (*b*) $v_{ctrl} = -0.720$, $p_{ext} = 4.06$; (*c*) $v_{ctrl} = -0.833$, $p_{ext} = 4.46$; (*d*) $v_{ctrl} = -0.875$, $p_{ext} = 4.65$. A lengthscale is provided by the circumferential lines on the tube wall which are spaced $\Delta z = 0.526$ apart.

the external pressure beyond the buckling pressure leads to a rapid collapse of the tube: for $p_{ext} = 4$, the control point has collapsed radially inwards by about 70% of the tube's undeformed radius; for $p_{ext} = 5.15$ the opposite walls come into contact when $v_{ctrl} = -(1 - h/(2R_0)) = -0.975$. The computation could only be carried out up to the first occurrence of opposite wall contact since the contact problem is not included in the present numerical model.

Figure 3 shows how the shape of the meniscus, which meets the tube wall at a constant contact angle of $\gamma = 10^\circ$, varies with the tube's deformation. For an axisymmetric tube (not shown), the meniscus is a spherical cap which meets the tube wall along the line $z = -0.818$. During the early stages of the tube's post-buckling deformation, when the cross-sections are approximately elliptical, the contact line moves in the negative z-direction in the plane $x = 0$ where the wall curvature is higher; it moves in the positive z-direction in the plane $y = 0$ where the tube wall is relatively flat. If the tube's cross-sections were to remain elliptical throughout the deformation then this trend would continue and two long thin 'tongues' would develop in the two regions of high wall curvature.

Figure 3 shows that this trend is reversed when the tube's cross-section begins to change to a dumb-bell shape: in the plane $x = 0$, the contact line moves in the positive z-direction and a narrow meniscus finger begins to develop in the most strongly collapsed part of the tube. This finger grows very rapidly along the tube's centreline in the negative z-direction as the tube's collapse increases.

The development of this finger is closely related to the fact that the meniscus is a surface of constant mean curvature. To explain this, we express the meniscus' curvature in terms of its principal radii of curvature on the tube's axis, i.e. $\kappa =$

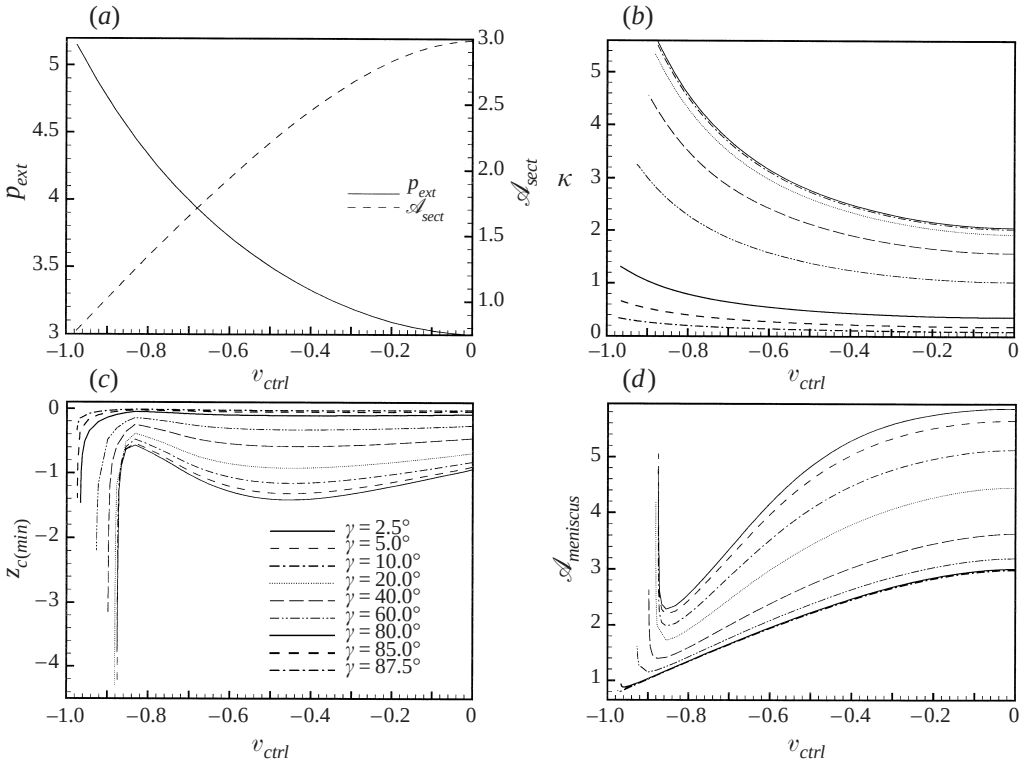

FIGURE 4. Characteristic parameters for menisci of various contact angles in a uniformly collapsing tube: (*a*) external pressure, p_{ext}, and the tube's cross-sectional area, $\mathscr{A}_{sect}$; (*b*) meniscus curvature, κ; (*c*) z-coordinate of 'lowest' point of the contact line, $z_{c(min)}$; and (*d*) meniscus surface area, $\mathscr{A}_{meniscus}$ – all plotted versus the tube's deformation, characterized by the radial displacement, v_{ctrl}, of the most strongly collapsed point on the tube wall. The legend for the linestyles in figure (*c*) applies to (*b*) and (*d*) also.

$1/R_x + 1/R_y$. As the tube collapses, the vertical distance between the opposite walls, $\mathscr{G} = 2(1 - h/(2R_0) + v_{ctrl})$, is reduced and for small $\mathscr{G}$ the meniscus' vertical radius of curvature, R_x, is enforced by the contact angle. Hence, $1/R_x \approx 2\cos\gamma/\mathscr{G}$, which grows very rapidly as the opposite walls approach each other. Equation (B 5), derived in Appendix B, shows that the curvature κ varies inversely with the tube's cross-sectional area, $\mathscr{A}_{sect}$, which decreases approximately linearly with v_{ctrl} (see figure 4*a*) and remains finite. The tube wall deforms with little circumferential extension, therefore the length $\mathscr{S}$ of the contact line's projection onto the (x, y)-plane remains approximately constant. Hence κ only grows slowly (see figure 4*b*) and the large increase in $1/R_x$ has to be compensated for by a decrease in $1/R_y$ which changes from a positive value (in figure 3*a*) through zero (in figure 3*b*) to increasingly large negative values (in figure 3*c*, *d*) thus causing the development of the finger. Ultimately, an asymptotic structure develops in which the two nearly straight sides of the long finger smoothly connect the finger tip of hyperbolic curvature to the parts of the meniscus in the two outer lobes which are relatively unaffected by the development of the finger and retain their initial elliptical curvature (see figure 3*d*).

Figure 4 (*b–d*) further illustrates this behaviour and also demonstrate the effect of variations in the contact angle. The meniscus curvature in the undeformed tube is given by $\kappa_0 = 2\cos\gamma/(1 - h/(2R_0))$ and figure 4 (*b*) shows that for all contact angles

the meniscus curvature increases to about twice that value before the finger begins to develop. Since the apices of the menisci are kept fixed at $z = 0$, the initial position of the contact line in the unbuckled tube is given by $z_{c0} = -[2/\kappa_0 - (1 - h/(2R_0)) \tan\gamma]$. Figure 4(*c*) shows how the 'lowest' point on the contact line, $z_{c(min)} = \min R_c^3(\varphi)$, initially moves into the negative z-direction and then reverses its direction when v_{ctrl} exceeds a value of $v_{ctrl} \approx 0.5$. Finally, the finger develops and grows rapidly, moving the 'lowest' point on the contact line in the negative z-direction as the tube's collapse increases. The development of the finger is delayed by an increase in the contact angle but it develops for all $\gamma < 90°$. The case $\gamma \to 90°$ is a singular limit since for $\gamma = 90°$ the meniscus' curvature vanishes and is independent of the cross-sectional shape. The limit $\gamma \to 0°$ is regular even though this case cannot be investigated with the present computational approach (see Appendix C). Finally, figure 4(*d*) shows that the meniscus' surface area (and hence its surface energy) decreases monotonically with increasing collapse until the development of the finger increases it sharply.

4.2. *Liquid bridges of minimum volume*

We will now consider the case in which the non-dimensional air–liquid surface tension σ is so large that the pressure jump over the two menisci which enclose the liquid bridge affects the deformation of the tube. We will determine the meniscus shapes and the minimum volume of fluid, $\mathscr{V}_{min}$, required to form an occluding liquid bridge in a buckled tube. In the physiological applications, $\mathscr{V}_{min}$ is an important parameter since it is directly related to the minimum initial thickness of the uniform liquid lining for which an occluding liquid bridge can develop. For a given tube shape, the liquid bridge containing the smallest volume of liquid is formed by two 'back-to-back' air–liquid interfaces which touch each other at one or more points. We will refer to this configuration as a minimal liquid bridge. In an axisymmetric tube of radius R, the minimal liquid bridge is formed by two spherical air–liquid interfaces and the enclosed volume is given by

$$\mathscr{V}_{min}^{(ax.)} = \frac{2\pi R^3}{3} \; \frac{2\sin^3\gamma + 3\cos^2\gamma - 2}{\cos^3\gamma}. \tag{21}$$

If the tube is elastic and deforms axisymmetrically, then the compression of the tube wall in the region where it is wetted by the liquid bridge will reduce its radius R and the minimal liquid bridge volume $\mathscr{V}_{min}^{(ax.)}$ slightly. Much larger reductions in $\mathscr{V}_{min}$ can presumably be achieved if the tube is allowed to buckle non-axisymmetrically. To investigate this case, we consider the deformation of a long tube which contains a single minimal liquid bridge, enclosed between two air–liquid interfaces which touch in the plane $z = 0$. Since the tube's deformation is symmetric in the z-direction, only one half of the tube and one meniscus have to be modelled. Symmetry boundary conditions for the tube's deformation were applied at $z = 0$ and far away from the meniscus at $z = -10$. The meniscus position was determined by the displacement constraint $z_{m(max)} = \max R_m^3 = 0$. Computations were carried out for a wide range of contact angles, external pressures and surface tensions.

Figure 5 shows two strongly collapsed tubes which contain a single minimal liquid bridge. In each case, only one half of the tube and one meniscus are shown since the configuration is symmetric about the plane $z = 0$. The external pressure acting on the tube shown in figure 5(*a*) is zero, $p_{ext} = 0$, and the tube is held in a strongly collapsed configuration by the large compressive load which the liquid bridge exerts on the tube wall. Hence, the tube re-opens quickly to an axisymmetric shape as one moves away from the pinched region. Since the width of the gap between the opposite

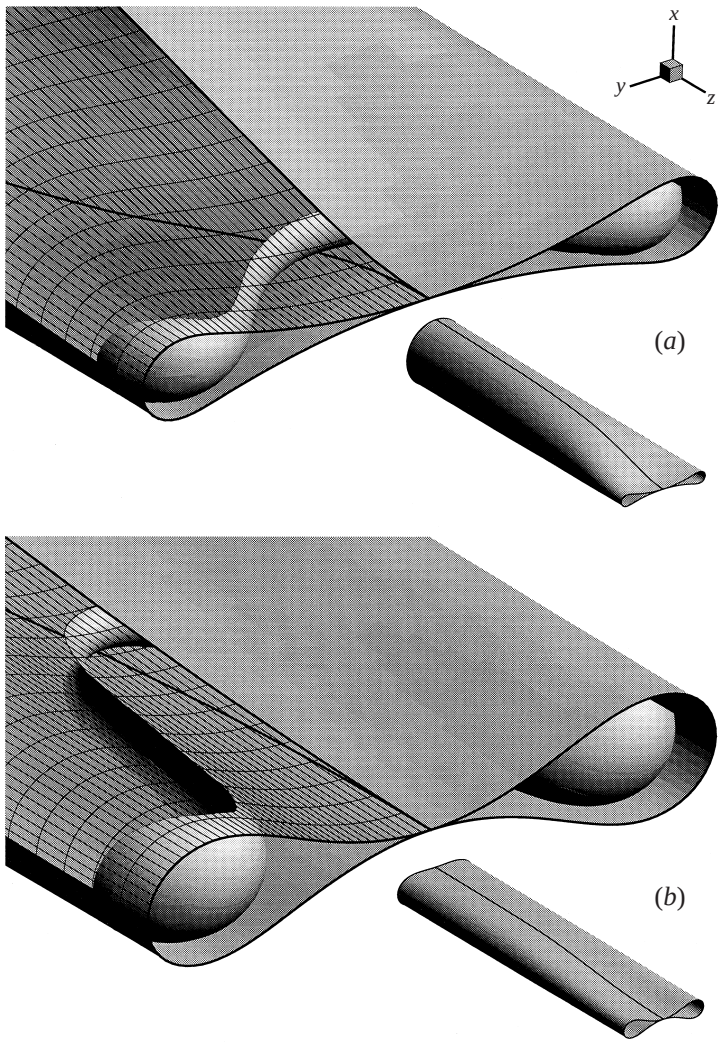

FIGURE 5. Two strongly collapsed tubes containing a minimal liquid bridge. The symmetrically deformed tubes were cut in the plane of symmetry ($z = 0$) and only one half of the tube and one meniscus are shown. The larger parts of the pictures show close-ups of the region containing the liquid bridge; the smaller pictures show the overall deformation of the tube. The circumferential lines on the tube wall are spaced $\Delta z = 0.174$ apart. $\gamma = 10°$. (*a*) $p_{ext} = 0$, $\sigma = 4.72$; (*b*) $p_{ext} = 3.5$, $\sigma = 0.69$.

walls increases rapidly with the axial distance from the tube's most strongly collapsed cross-section, the meniscus only develops a relatively small finger in the central part of the tube.

Conversely, the tube shown in figure 5(*b*) is subject to an external pressure in excess of the tube's buckling pressure. Therefore, the tube remains strongly collapsed over its entire length and the small width of the gap between the opposite walls leads to the development of a strongly pronounced meniscus finger. A much smaller surface tension is required to hold the tube in this strongly collapsed configuration.

We will now systematically investigate the range of parameter values for which the forces generated by a minimal liquid bridge are sufficient to hold the tube in

a buckled shape and document the corresponding values of $\mathscr{V}_{min}$. Since we have already established the range of external pressures for which the tube collapses ($3 < p_{ext} < 5.15$ for $\sigma = 0$), we will first consider the effect of variations in the surface tension (variations in p_{ext} for $\sigma =$ const. will be examined in § 4.3.2). For this purpose a series of computations was carried out in which the values of the external pressure and the contact angle were held at constant values while the tube's deformation was controlled by varying the surface tension. The two air–liquid interfaces were kept in the 'minimal liquid bridge configuration' by applying the displacement constraint $z_{m(max)} = 0$.

In order to explain the fairly complicated dependence of $\mathscr{V}_{min}$ on the surface tension (presented below in figures 7 and 8) we will first analyse the results of one such computation by interpreting them as if they were the outcome of an actual experimental procedure. It should be noted that such an experiment would be difficult to perform since one would not only have to carefully control the surface tension but also constantly adjust the fluid volume in the liquid bridge to keep the opposite air–fluid interfaces in contact. Figure 6 shows the results of a computation for $p_{ext} = 0$ and $\gamma = 10°$. The tube's deformation, characterized by the radial wall displacements along the major and minor axes in the most strongly collapsed cross-section in the plane $z = 0$, is plotted against the surface tension, i.e. $v_{ctrl}(\sigma)|_{z_{m(max)}=0}$. The straight dashed line of small negative slope corresponds to the tube's axisymmetric deformation. For $\sigma = 0$ the tube is undeformed, $v_{ctrl} = 0$. With increasing surface tension, the compressive load on the wetted part of tube wall increases and the control points are displaced radially inwards by the same small amount. At $\sigma = 9.10$ (point 'A') the axisymmetric solution becomes unstable and the tube buckles: the control point on the tube's major axis is displaced radially outwards (giving rise to the upper branch with positive v_{ctrl}) while the other control point collapses radially inwards (corresponding to the lower branch with negative v_{ctrl}). The diagram shows that the system undergoes a subcritical bifurcation when the tube buckles: if the surface tension were kept constant during the buckling (and if it were indeed possible to perform an experiment in this way), then the tube would jump into a strongly collapsed configuration (point 'C') in which the control point on the tube's minor axis has collapsed radially inwards by about 75 % of the tube's radius. This behaviour (known as 'snap-through' buckling) is well known in the solid mechanics literature (see e.g. Kirstein & Wenk 1956) and has been reported previously in other fluid–structure interaction problems (Heil & Pedley 1996; Heil 1997). The occurrence of the snap-through is due to the fact that the tube's bending stiffness is much smaller than its extensional stiffness. In the axisymmetric state, all wall deformations are accompanied by a circumferential compression or extension of the tube wall. Therefore, only small wall displacements are required to generate the elastic restoring forces required to balance the compressive load produced by the liquid bridge. Once the tube buckles, the main contribution to the wall stiffness comes from its much smaller bending stiffness and a balance between the compressive meniscus forces and the restoring elastic forces can only be achieved if (i) the meniscus forces are reduced (by decreasing the surface tension – this corresponds to the backwards curving part of the post-buckling curve from 'A' to 'B') or (ii) if the wall is allowed to deform strongly to generate sufficiently large bending moments (this corresponds to a jump along the line of constant surface tension from 'A' to 'C').

Once the tube has reached this strongly collapsed configuration, a further increase in its deformation requires an increase in the compressive load which the liquid bridge exerts on the tube wall. To some extent this is provided automatically since the meniscus curvature increases with increasing collapse of the tube (similar to

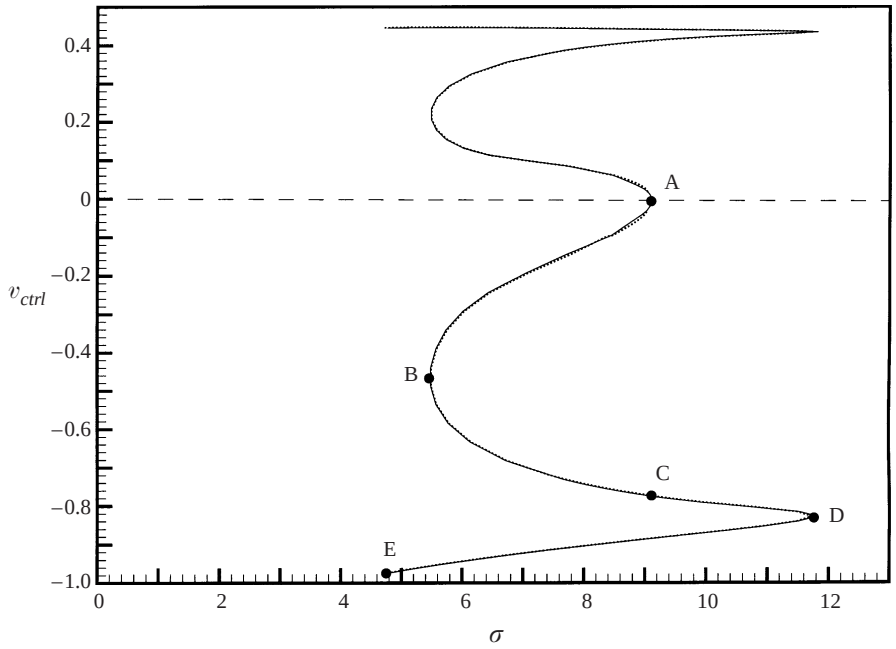

FIGURE 6. Bifurcation diagram, $v_{ctrl}(\sigma)|_{z_{m(max)}=0}$, for a tube containing a minimal liquid bridge: the two control displacements (the radial displacements of the tube wall along the major ($v_{ctrl} > 0$) and minor ($v_{ctrl} < 0$) axes of the tube's most strongly collapsed cross-section) are plotted versus the surface tension. The two air–liquid interfaces are kept in contact such that they enclose a minimal liquid bridge. The dashed line represents the axisymmetric pre-buckling deformation, the solid line corresponds to the post-buckling deformation. The dotted line was obtained with a finer spatial discretization of the shell and meniscus equations. $p_{ext} = 0$ and $\gamma = 10°$.

figure 4 *b*). Hence, the pressure jump over the air–liquid interfaces increases with the tube's collapse even if the surface tension remains constant. However, the wall area which is wetted by the liquid bridge (and hence exposed to the compressive load) initially decreases, especially in the region where the tube wall buckles inwards (as shown in § 4.1). Therefore, a further collapse of the tube can only be achieved by increasing the surface tension (this corresponds to the path from 'B' via 'C' to 'D'). When the tube's collapse is increased past point 'D', the meniscus finger develops and rapidly increases the wetted wall area in the central, inwardly collapsing part of the tube. This increases the compressive load on the tube wall so rapidly that a monotonic increase in the tube's deformation can only be achieved if the surface tension is reduced, giving rise to the path from 'D' to 'E'. As mentioned before, the computation was terminated when opposite wall contact occurred for the first time ($v_{ctrl} = -0.975$, corresponding to the configuration shown in figure 5 *a*) since the wall contact was not modelled.

Figure 7 shows how this behaviour manifests itself in the graphs for the minimal liquid bridge volume, $\mathscr{V}_{min}$, as a function of the surface tension, σ. The different linestyles correspond to different contact angles and for all cases the external pressure was kept constant at $p_{ext} = 0$. The nearly straight lines of small negative slope correspond to the axisymmetric configurations and illustrate the behaviour anticipated earlier: at $\sigma = 0$ the lines intersect the volume axis at the value predicted by (21) and $\mathscr{V}_{min}$ decreases slightly with increasing σ. Menisci with larger contact angles form shallower liquid bridges of smaller volume.

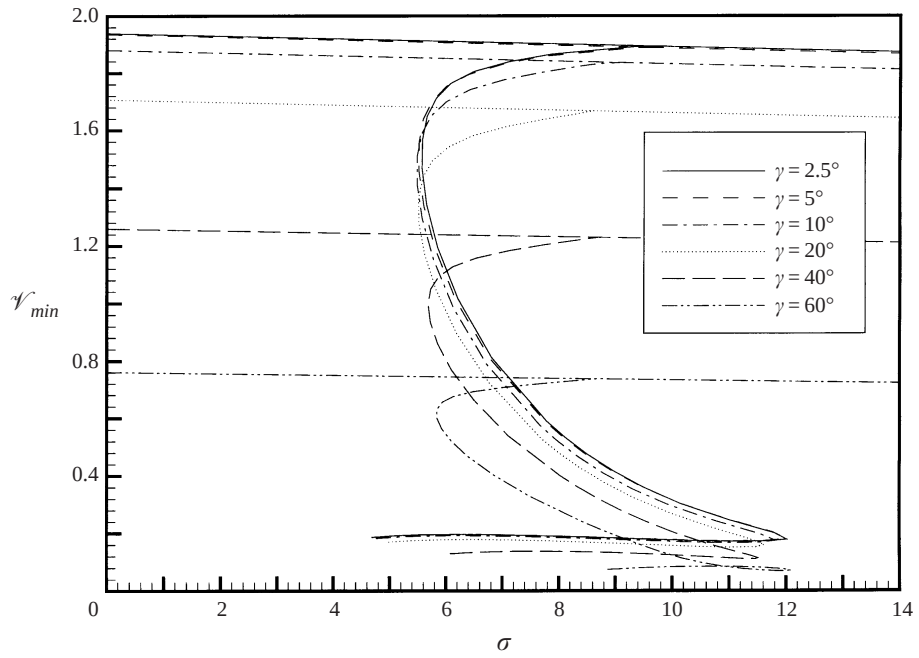

FIGURE 7. Minimal liquid bridge volume, $\mathscr{V}_{min}$, as a function of the surface tension, σ, for $p_{ext} = 0$ and various contact angles γ. The nearly straight lines of small negative slope correspond to axisymmetric pre-buckling configurations, the other lines represent buckled configurations.

In a certain range of surface tensions (between $\sigma \approx 5.5$ and $\sigma \approx 9.5$), there exist up to three buckled equilibrium configurations (with different values of $\mathscr{V}_{min}$) in which the meniscus forces balance the restoring wall forces. $\mathscr{V}_{min}$ depends on the tube's cross-sectional area and on the average thickness of the liquid bridge. The tube's cross-sectional area decreases monotonically with the tube's collapse and in the early stages of the buckling, the average liquid bridge thickness only changes very little. Hence, $\mathscr{V}_{min}$ decreases monotonically with increasing collapse until the meniscus finger begins to develop. Following this, the rapidly increasing volume of fluid contained in the finger compensates for the further reduction in cross-sectional area and $\mathscr{V}_{min}$ remains approximately constant. The minimal liquid bridges of smallest volume are formed in strongly collapsed tubes in which the meniscus finger has just started to develop. The volume of fluid required to form these liquid bridges is about 10 % of that required to form an occluding liquid bridge in the corresponding axisymmetric configuration.

Figure 8 illustrates the dependence of $\mathscr{V}_{min}$ on the external pressure, p_{ext}: if we increase the external pressure, the tube can only withstand smaller compressive forces from the liquid bridge before it buckles. Hence for increased external pressures, buckling (and the corresponding reduction in $\mathscr{V}_{min}$) occurs at lower values of the surface tension. For $p_{ext} = p_{ext}^{(crit)} = 3$, only an infinitesimally small surface tension is required to induce the tube's buckling. For external pressures in excess of the buckling pressure ($p_{ext} > 3$), the tube remains collapsed (and $\mathscr{V}_{min}$ considerably smaller than the value for the axisymmetric tube) even for $\sigma \to 0$. Note that for larger values of the external pressure, the meniscus finger is much more pronounced as illustrated in figure 5(*b*). In these cases the rapid increase in the volume of fluid contained in the finger more than compensates for the reduction in the tube's cross-sectional area

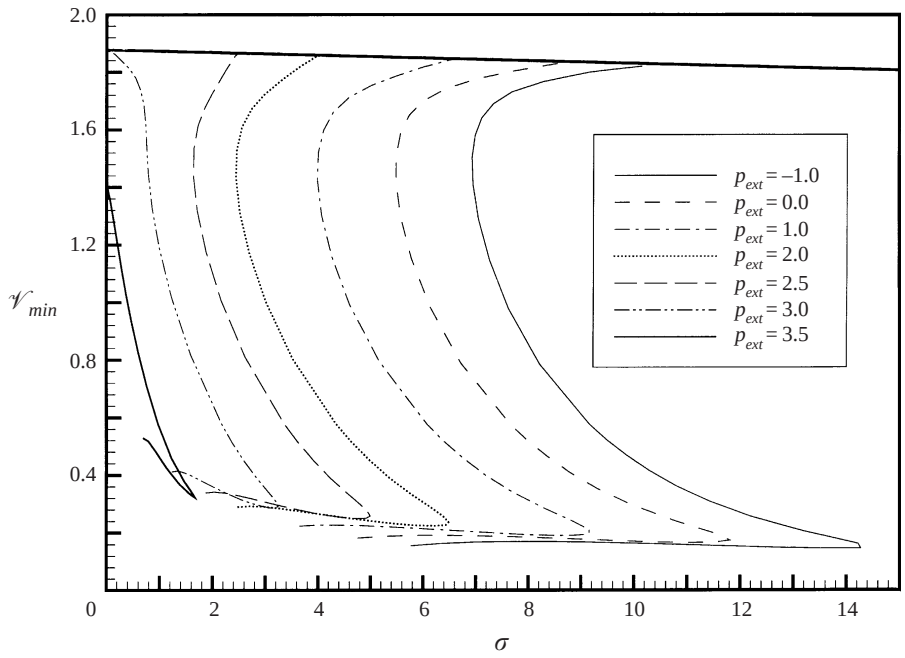

FIGURE 8. Minimal liquid bridge volume, $\mathscr{V}_{min}$, as a function of the surface tension, σ, for $\gamma = 10^\circ$ and various p_{ext}. The nearly straight lines of small negative slope which correspond to axisymmetric pre-buckling configurations overlap; the other lines represent buckled configurations.

as the tube's collapse increases and $\mathscr{V}_{min}$ has its minimum value shortly after the meniscus finger begins to develop.

4.3. *The stability of minimal liquid bridges*

The results of the previous section indicate that for many combinations of the control parameters (contact angle, surface tension and external pressure), there exist multiple buckled equilibrium configurations (with different values of $\mathscr{V}_{min}$). We will now investigate which (if any) of these buckled configurations are stable to quasi-steady perturbations since only those configurations which fulfil this criterion would be realizable in an experiment. For this purpose we first have to find a suitable definition of 'stability' since most minimal liquid bridges are obviously unstable to a particular class of disturbances: they can be destroyed by perturbations which re-open the tube since the volume of fluid contained in a minimal liquid bridge will generally not be sufficient to form an occluding liquid bridge in a slightly less collapsed tube.

4.3.1. *The stability of axisymmetric minimal liquid bridges*

To develop a suitable concept of stability we will first examine the deformation characteristics of a tube which contains a minimal liquid bridge in its undeformed axisymmetric configuration ($\mathscr{V} = \mathscr{V}_{min}^{(ax.)} = 1.87$ for $\gamma = 10^\circ$). As before, we will characterize the tube's deformation by the radial displacements of the material points on the major and minor axes of the tube's most strongly collapsed cross-section. However, we will now consider a physically realizable experiment and keep the volume of fluid in the liquid bridge, the contact angle and the surface tension constant and study the tube's deformation as we vary the external pressure. The corresponding bifurcation diagram, $v_{ctrl}(p_{ext})|_{\mathscr{V}=\mathscr{V}_{min}^{(ax.)}=const.}$, is shown in figure 9. Let us

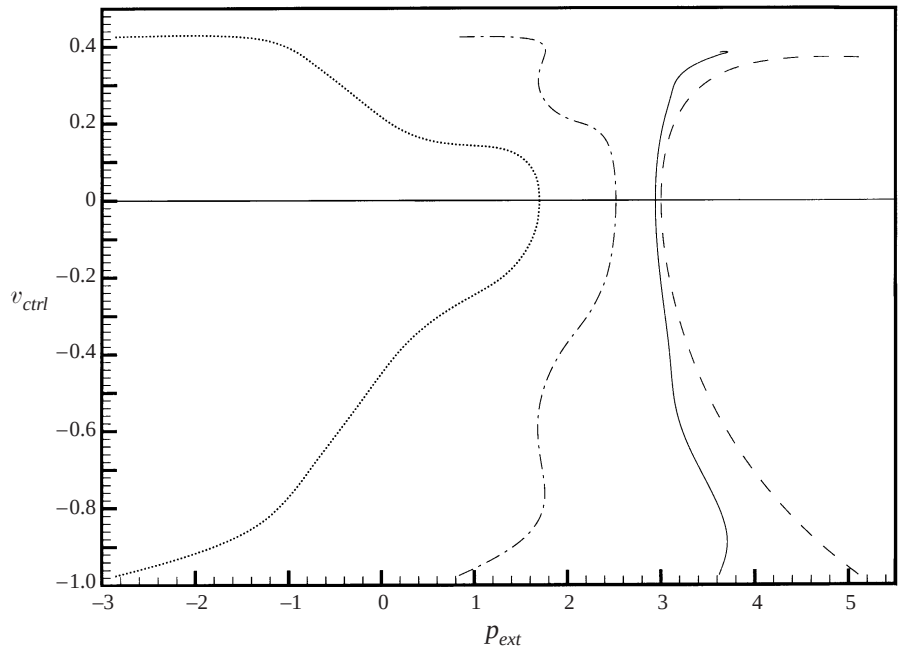

FIGURE 9. Bifurcation diagram, $v_{ctrl}(p_{ext})|_{\mathscr{V}=\mathscr{V}_{min}^{(ax.)}=const.}$, for $\gamma = 10°$ and constant liquid bridge volume $\mathscr{V}^{(ax.)} = 1.87$. Dashed line: $\sigma = 0$; solid line: $\sigma = 0.5$; dash-dotted line: $\sigma = 2.5$; dotted line: $\sigma = 5.0$. The four nearly horizontal lines (corresponding to the axisymmetric pre-buckling configurations) overlap.

first identify the reference case, discussed in § 4.1, in which the surface tension (and the pressure jump over the air–liquid interfaces) vanishes, $\sigma = 0$. For $p_{ext} = 0$ the tube is undeformed, $v_{ctrl} = 0$. Positive external pressures in the range $p_{ext} < p_{ext}^{(crit.)} = 3$ compress the tube axisymmetrically, giving rise to the solid straight line with small negative slope. For $p_{ext} > p_{ext}^{(crit.)} = 3$ the axisymmetric state is unstable and the tube's non-axisymmetrically buckled states are described by the upper and lower branches of the dashed curve. The diagram indicates that for $\sigma = 0$ the tube buckles via a supercritical bifurcation and that the system has a positive stiffness throughout its deformation: an increase in external pressure is required to increase the tube's collapse. Hence, all buckled configurations are stable in the sense that small disturbances to the tube's shape (during which all other parameters are held constant) lead to a force imbalance which would tend to return the tube wall to its undisturbed shape (see e.g. Thompson & Hunt 1973; Michael 1981).

The other curves shown in figure 9 indicate how finite surface tension affects the tube's deformation characteristics. First, the diagram shows that an increase in surface tension lowers the tube's buckling pressure, $p_{ext}^{(crit.)}$, since it increases the compression of the tube. Second, since the tube's cross-sectional area decreases with increasing collapse, the liquid bridge thickness has to increase in order to conserve the volume of fluid in the liquid bridge. This increases the wall area which is wetted by the liquid bridge (and thus exposed to its compressive load) and leads to a destabilization which manifests itself in the larger slope of the post-buckling curves, i.e. in a reduction of the system's stiffness: a smaller increase in p_{ext} is required to achieve the same increase in collapse. A further destabilization occurs when the meniscus finger begins to develop (when $v_{ctrl} \lesssim -0.8$) and further increases the wall area which is wetted by the liquid

bridge. Figure 9 shows that the destabilization can be so strong that parts of the post-buckling curve become branches of negative stiffness on which a decrease in external pressure would be required to monotonically increase the tube's deformation. The configurations which correspond to these parameter values are unstable in the sense that a perturbation to the tube's shape leads to a force imbalance which tends to increase the tube's collapse even further.

For a liquid bridge with a small surface tension of $\sigma = 0.5$, the tube's collapse increases monotonically with the external pressure until the destabilization due to the development of the meniscus finger creates a limit point on the post-buckling path (at $p_{ext} = p_{ext}^{(limit)} = 3.70$). If the pressure were increased beyond that value, the strong compressive load acting on the tube wall could only be balanced if the tube collapsed much more strongly into a configuration in which opposite wall contact increases the wall stiffness sufficiently.

For larger surface tensions, $p_{ext}^{(limit)}$ coincides with the buckling pressure $p_{ext}^{(crit.)}$. In these cases, the loss of stability of the axisymmetric configuration would be followed by a large (quasi-steady) 'jump' into a very strongly collapsed configuration with opposite wall contact over a large part of the tube wall. For the intermediate surface tension of $\sigma = 2.5$, a short stable segment exists on the post-buckling curve in the range $1.64 < p_{ext} < 1.70$. Since this pressure range lies below the buckling pressure, $p_{ext}^{(crit.)} = 2.49$, the corresponding configurations could only be realized by applying a finite perturbation to the (linearly stable) axisymmetric configuration. For the largest surface tension shown ($\sigma = 5.0$), the entire post-buckling path is unstable.

4.3.2. *The stability of non-axisymmetric minimal liquid bridges*

We are now able to analyse the stability of minimal liquid bridges in non-axisymmetrically buckled tubes. For this purpose we first re-examine the deformation characteristics of a tube containing a minimal liquid bridge whose volume we constantly adjust such that the air–liquid interfaces stay in contact as the tube deforms. However, as opposed to the case considered in § 4.2, we now keep σ constant and vary p_{ext} as the control parameter. Figure 10(*a*) maps out the equilibrium paths, $v_{ctrl}(p_{ext})|_{z_{m(max)}=0}$, for this case. If we interpret these data as the outcome of a hypothetical experiment then we observe the now familiar destabilizing effect of increasing surface tension and the further destabilization of the system when the meniscus finger begins to develop. Figure 10(*b*) shows the corresponding variation of $\mathscr{V}_{min}$ and shows that for small surface tensions (for which the tube's collapse is dominated by p_{ext} so that the tube collapses over its entire length, as shown in figure 5 *b*), the development of the strongly pronounced finger leads to a sharp increase in $\mathscr{V}_{min}$ as the collapse increases beyond $v_{ctrl} \lesssim -0.8$.

To examine the stability of these equilibrium configurations to physically realizable quasi-steady perturbations (i.e. perturbations during which the volume of fluid in the liquid bridge is kept constant) we need to consider the system's response to small perturbations to the tube's shape. The system's stability is determined by the direction of the force imbalance caused by these perturbations and hence by the slope of the corresponding constant-volume deformation characteristics. An example of this (for the case $\sigma = 3.0$) is given in figure 11 where only the lower branch of the post-buckling curve, $v_{ctrl}(p_{ext})|_{z_{m(max)}=0}$, is shown. Each point on this equilibrium path is intersected by a second path, $v_{ctrl}(p_{ext})|_{\mathscr{V}=\mathscr{V}_{min}=const.}$, which represents the tube's deformation characteristics under constant liquid-bridge volume. The slope of this curve was determined by finite differencing and is represented by the arrows which point in the direction of increasing collapse. Increasing collapse increases the liquid bridge thickness, therefore

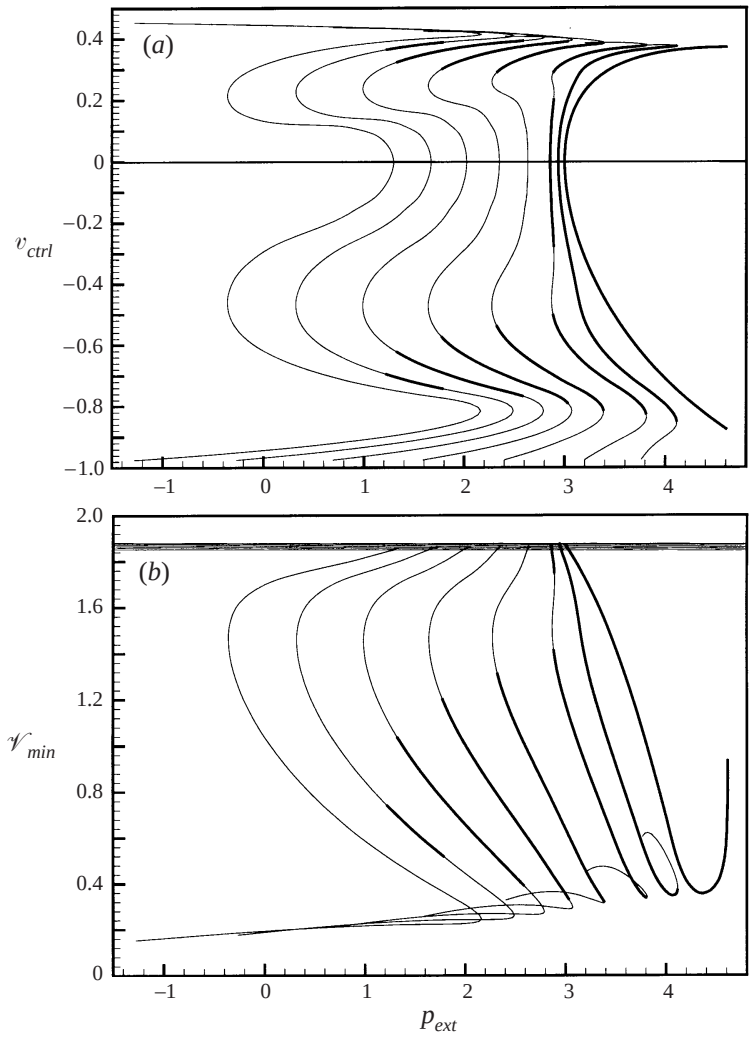

FIGURE 10. Diagrams illustrating the stability of elastic tubes containing minimal liquid bridges: (*a*) shows the bifurcation diagram $v_{ctrl}(p_{ext})|_{z_{m(max)}=0}$, (*b*) shows the minimum liquid bridge volume $\mathscr{V}_{min}$ as a function of the external pressure p_{ext}. The two air–liquid interfaces are kept in contact such that they enclose a minimal liquid bridge and the surface tension σ is kept constant along the curves. The thickened parts of the post-buckling curves correspond to configurations which are stable to quasi-steady perturbations during which the liquid bridge volume remains constant. $\sigma = 0$, 0.5, 1.0, 2.0, 3.0, 4.0, 5.0 and 6.0, increasing from right to left. The nearly straight lines of small negative slope represent axisymmetric configurations.

the line $v_{ctrl}(p_{ext})|_{z_{m(max)}=0}$ separates liquid bridges of finite thickness from (hypothetical) configurations in which the two menisci intersect. Forward pointing arrows represent configurations in which the system has positive stiffness and is stable. The system is unstable to quasi-steady constant-volume perturbations at points at which the equilibrium curve is intersected by backwards pointing arrows. The stable part of the post-buckling curve is indicated by the thickened line. The same procedure was used to identify the stable parts of the post-buckling curves in figure 10.

For hypothetical perturbations during which the opposite air–liquid interfaces were kept in contact, only the backward curving parts of the equilibrium paths in figure

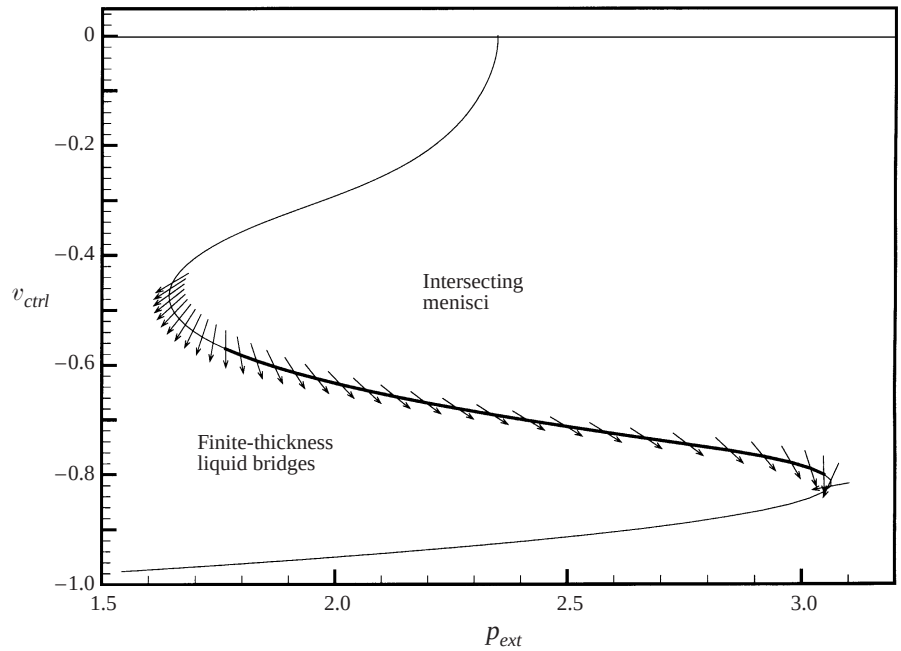

FIGURE 11. Lower part of the bifurcation diagram for a tube containing a minimal liquid bridge with $\sigma = 3.0$: the radial displacement along the tube's minor axis in its most strongly collapsed cross-section is plotted versus the external pressure, p_{ext}. The vectors indicate the slopes of the curves corresponding to constant liquid bridge volume, $v_{ctrl}(p_{ext})|_{\mathcal{V}=\mathcal{V}_{min}=const.}$. The stable post-buckling parameter range (identified by the forward pointing arrows) is marked with a thicker line.

10(*a*) would be unstable. The additional restriction of constant liquid-bridge volume leads to a further destabilization due to the increase in wetted wall area during such perturbations. Figure 10 shows that the strength of the destabilization increases with increasing surface tension: for a small surface tension of $\sigma = 0.5$, nearly the entire forward curving part of the equilibrium path remains stable; for $\sigma = 5.0$, only a small fraction of the forward curving path is stable; and for $\sigma = 6.0$ all buckled configurations (without opposite wall contact) are unstable.

As mentioned above, minimal liquid bridges represent extreme configurations since they are always unstable to perturbations which decrease the tube's collapse and thus rupture the liquid bridge. In this sense, liquid bridges of small but finite minimal thickness, t, are more stable. However, an increase in the liquid bridge thickness also increases the compressive load on the tube wall and thus destabilizes the system in the sense that, in stable regimes, smaller external pressures are required to achieve the same degree of collapse. Hence, the deformation characteristics for a tube containing a liquid bridge of small but finite thickness, $v_{ctrl}(p_{ext})|_{z_{m(max)}=-t/2}$, lie to the left of the curves for the minimal liquid bridges, as indicated in figure 11.

It should be noted that a completely rigorous stability analysis has to be based on the limit points of the $\mathcal{V}_{tot}(p_{ext})$ curve, where $\mathcal{V}_{tot}$ is the total volume contained in the tube (i.e. the sum of the volumes in its air-filled and liquid-filled parts); see Maddocks (1987). However, the predictions for the stable and unstable parameter regimes obtained from these curves are identical to those obtained from the bifurcation diagrams presented here. Therefore, the $\mathcal{V}_{tot}(p_{ext})$ diagrams are not shown here. The author is grateful to one of the referees for pointing out this potential shortcoming of the analysis presented above.

5. Discussion

We will now consider the implications of the above results (and their limitations) for the biological problem that originally motivated this study. Halpern & Grotberg (1992) provide estimates for the typical dimensions and properties of the liquid-lined terminal bronchioli of the lung ($R_0 \approx 2.5 \times 10^{-2}$ cm, $h \approx 2.5 \times 10^{-3}$ cm, $E = 6.0 \times 10^4$ dynes cm^{-2}, $\sigma^* = 20$ dynes cm^{-1}). Note that these dimensional parameters affect the system's behaviour only via the non-dimensional parameter $\sigma = \sigma^*/(K\ R_0)$ which represents the ratio of the typical pressure jump over the menisci to the tube's bending stiffness. In diseases, σ, and hence the susceptibility of the airways to collapse, can be affected by changes to the surface tension and by changes to the wall stiffness. The values quoted above correspond to a value of $\sigma = 120$. Note that the deformation characteristics of tubes containing a minimal liquid bridge in their axisymmetric state (see figure 9) showed that a comparatively moderate surface tension of $\sigma = 5$ leads to a significant reduction in the tube's buckling pressure. Furthermore, a surface tension of $\sigma = 5$ is already sufficient to make all buckled configurations without opposite wall contact unstable, indicating that the buckled tube would collapse into a very strongly deformed configuration with opposite wall contact. The much larger value of σ in the physiological problem would therefore suggest that axisymmetric liquid bridges in the terminal bronchioli are strongly unstable to non-axisymmetric disturbances of the tube wall. If perturbed, the airway walls would collapse strongly and in the process spread out the fluid contained in the liquid bridge over a large region. This prediction is consistent with the usual assumptions made in the modelling of the airway re-opening problem (Gaver *et al.* 1990). However, it should be noted that the precise nature of the collapse in the physiological problem will also be influenced by the parenchymal tethering (see e.g. Yap *et al.* 1994) which has not been included in the present model.

Potential limitations of the quasi-steady stability analysis presented in § 4.3 lie in the neglected contact angle hysteresis (see e.g. Michael 1981). However, the parameter studies in which variations of the contact angle were considered showed that it did not significantly change the system's overall behaviour. The neglect of gravitational effects in the present study seems justified in view of the small Bond number $Bo = \rho g R_0^2/\sigma = 0.03$ (for $g = 9.81\,\mathrm{m\,s^{-2}}, \rho = 1000\,\mathrm{kg\,m^{-3}}$) in the terminal bronchioli.

Motivated by the models used in studies of airway re-opening (Gaver *et al.* 1990), the present study has only considered cases in which the tube buckles in a two-lobed mode. However, it is well known (see e.g. Yamaki 1984 and Heil 1996) that thin-walled cylindrical tubes can buckle with a higher number of circumferential waves. The most unstable circumferential wavenumber for small perturbations to the axisymmetric state increases as either the tube's length or the fraction of the tube's length which participates in the buckling decreases. The shell displacement boundary conditions which were used in the present study (axially periodic with a large wavelength) are certain to make $N = 2$ the most unstable wavenumber, provided the surface tension is not so high that the tube's collapse becomes very strongly localized near the liquid bridge. This condition could be achieved by subjecting the tube to a large negative external pressure (which would tend to inflate it overall) and to induce its collapse by a liquid bridge of large surface tension and large contact angle, such that a large compressive load is applied over a small wetted area. No formal stability analysis was carried out since the most unstable wavenumber for the physiological problem would be determined by the time-dependent evolution from an axisymmetric state, in which the liquid bridge has not yet been formed.

The computations in § 4.2 showed that the minimum volume of fluid required to form an occluding liquid bridge in a buckled elastic tube can be as low as 10% of the fluid volume required to occlude an axisymmetric tube. It should, however, be stressed that somewhat larger fluid volumes would presumably be required to form occluding liquid bridges from an initially axisymmetric liquid lining. This phenomenon was documented by Kamm & Schroter (1989) and Everett & Haynes (1972) in their studies of the formation of liquid bridges in rigid axisymmetric tubes. Their experiments gave $\mathscr{V}_{min}^{(exp)} \approx 5.6R^3$ and $\mathscr{V}_{min}^{(exp)} \approx 5.47R^3$, respectively. Both values are substantially larger than the theoretical minimal value $\mathscr{V}_{min}^{(ax.)} = 2\pi/3R^3$ for zero contact angle.

Two scenarios for the formation of non-axisymmetric liquid bridges in the physiological system are conceivable. (i) The liquid lining in the axisymmetric tube first undergoes the axisymmetric Rayleigh instability, accompanied by the corresponding axisymmetric wall deformation (as analysed by Halpern & Grotberg 1992, 1993), until an axisymmetric liquid bridge is formed in the tube. Based on the results of the present study, we would expect this to be immediately followed by an elastic instability during which the tube collapses strongly, while spreading out the (relative large) volume of fluid in the liquid bridge. (ii) The axisymmetric tube undergoes an elastic instability during the early stages of the axisymmetric evolution of the combined fluid–elastic instability *before* an occluding liquid bridge has been formed. This would require smaller volumes of fluid but would only be possible if the elastic instability was 'stronger' than the stability of the axisymmetric air–liquid interface to non-axisymmetric perturbations. The snap-through behaviour of the tube wall, found in the present study, makes this condition likely to be fulfilled: if the timescale for the (dynamic) snap-through buckling of the tube wall is shorter than the timescale on which the relatively thin liquid film re-distributes itself along the tube wall, then the rapid non-axisymmetric collapse could bring the opposing air–liquid interfaces into contact and thus initiate the formation of an occluding liquid bridge.

It should be noted that occluding liquid bridges are not the only possible final steady states that can develop from the instability of the initial liquid lining. Other non-occluding static distributions of fluid along the buckled tube wall (e.g. similar to those studied by Jensen 1996), are conceivable.

The results of the present study motivate an analysis of two problems: (i) the inclusion of a model for the opposite wall contact, which will enable us to investigate the strongly collapsed states which we found to be the only stable configurations for sufficiently large surface tensions; (ii) an investigation of the time-dependent formation of non-axisymmetric liquid bridges in elastic tubes and, in particular, their evolution from the initially axisymmetric state. Work on both problems is currently in progress.

6. Summary

The main results of this study are as follows: (i) menisci in uniformly collapsed elastic tubes develop a finger along the tube's centreline as the opposite walls approach each other; (ii) for a wide range of control parameters (the contact angle and the non-dimensional values of surface tension and external pressure) the compressive forces generated by the liquid bridge are strong enough to hold the elastic tube in a buckled configuration; (iii) the compressive forces generated by the liquid bridge are strongly enhanced by the development of the meniscus finger; (iv) for many parameter combinations, multiple minimal liquid bridges exist in tubes of varying degree of collapse; (v) only a small subset of these equilibrium configurations is stable

to quasi-steady perturbations; (vi) for sufficiently large surface tensions all buckled equilibrium configurations (without opposite wall contact) are unstable. For such parameters, the only stable configurations are very strongly collapsed tubes in which the opposite wall contact has increased the wall stiffness sufficiently to balance the strong compressive forces generated by the liquid bridge.

The author wishes to thank Professor T. J. Pedley, Dr Oliver Jensen, Andrew Hazel and Harvey Williams for many enjoyable and helpful discussions. Financial support was provided by an EPSRC fellowship.

Appendix A. The spine origins for strongly collapsed tubes

In § 3 we decomposed the vector to a point on the meniscus into the vectors $\boldsymbol{B}$ and $w\boldsymbol{S}$, such that $\boldsymbol{B}$ determines the origin for the meniscus displacement, w, along the spine $\boldsymbol{S}$; see figure 2. Equations (14) and (15) provided a simple mapping between the two meniscus surface coordinates ζ_α and the coordinates of the spine origin $\boldsymbol{B}$ for a contact line parametrization, $\boldsymbol{R}_c(\varphi)$, given by (6). This mapping is illustrated in figure 12 (*a*): Every point P in the ζ_α-domain is associated with one reference point on the contact line. The reference point is determined by its coordinate φ which is chosen as $\varphi = \varphi_P = \arctan(\zeta_1/\zeta_2)$. We locate the image point P' in the (x, y)-domain on the straight line connecting the origin of the (x, y)-coordinate system with the reference point, $\boldsymbol{R}_c(\varphi_P)$, on the contact line. The radial distance of P' from the origin is a linear function of the parameter $\rho = (\zeta_1^2 + \zeta_2^2)^{1/2} \in [0, 1]$ such that $\rho = 0$ corresponds to the origin and $\rho = 1$ to a point on the contact line. P' determines the (x, y)-coordinates of the spine origin $\boldsymbol{B}$. The line $\overline{0P'}$ forms an angle $\hat{\varphi}$ with the y-axis. In a strongly collapsed cross-section, such as the one shown in figure 12 (*b*), this mapping will fail since multiple points on the contact line share the same polar angle $\hat{\varphi}$.

The modified mapping, devised to avoid this problem, is illustrated in figure 12 (*b*): we split the ζ_α-domain into two regions which are separated by the line $\zeta_2 = \cos\varphi_{tr}$ ($\varphi_{tr} = 35^\circ$ proved a good choice and was used in all computations). Points in the shaded region in the ζ_α-domain (where $\zeta_2 > \cos\varphi_{tr}$) are mapped onto lines which emanate from the central point C' in the (x, y)-domain. The coordinates of C' were chosen as $(x_{C'}, y_{C'}) = (0, R_c^2(\varphi_{tr}))$. All other points in the ζ_α-domain are mapped onto straight lines which are parallel to the x-axis.

This is achieved by constructing the spine origin $\boldsymbol{B}$ as follows:

For all points P in the ζ_α-domain for which $\zeta_2 > \cos\varphi_{tr}$ (e.g. P_1 in figure 12 (*b*)), we determine the auxiliary angle $\tilde{\varphi}$ from

$$\tan\tilde{\varphi} = \frac{\zeta_1}{\zeta_2 - \cos\varphi_{tr}} \tag{A 1}$$

and use this to obtain the reference angle φ_P from

$$\tan\tilde{\varphi} = \frac{\sin\varphi_P}{\cos\varphi_P - \cos\varphi_{tr}}, \tag{A 2}$$

the appropriate solution of which is

$$\sin\varphi_P = \frac{\sin(2\tilde{\varphi})}{2}\left(\frac{(1 - \cos^2(\varphi_{tr})\sin^2(\tilde{\varphi}))^{1/2}}{\cos(\tilde{\varphi})} - \cos(\varphi_{tr})\right). \tag{A 3}$$

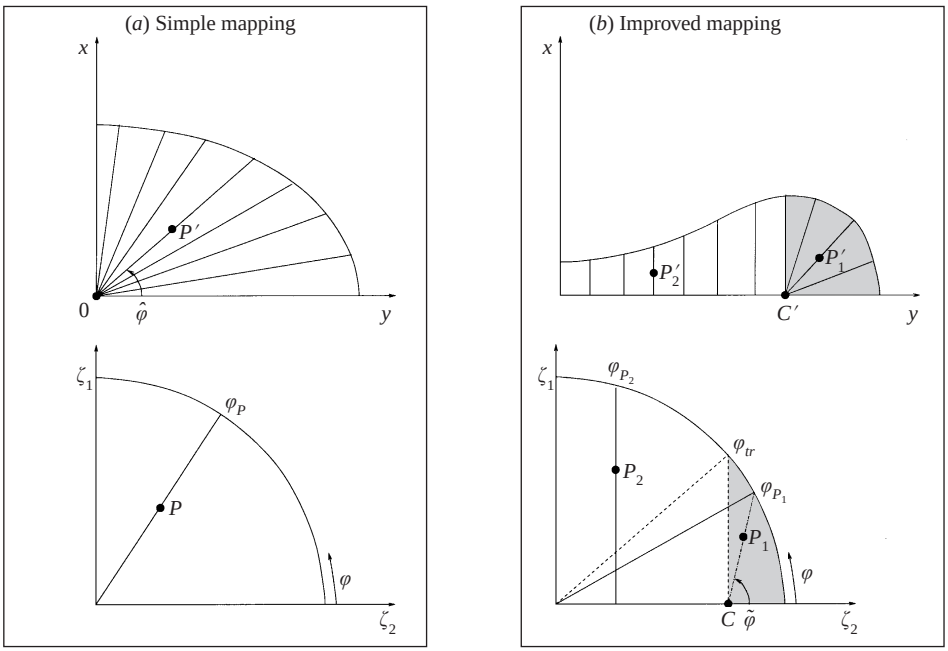

FIGURE 12. Sketch illustrating the mapping between the meniscus surface parameters ζ_α and the spine origin $\boldsymbol{B}$ for moderately and strongly collapsed cross-sections.

We control the radial distance of P' from C' by choosing

$$\rho = \left(\frac{\zeta_1^2 + (\zeta_2 - \cos\varphi_{tr})^2}{\sin^2\varphi_P + (\cos\varphi_P - \cos\varphi_{tr})^2} \right)^{1/2} \tag{A 4}$$

and choose the spine origin $\boldsymbol{B}$ as

$$B^1 = \rho R_c^1(\varphi_P), \tag{A 5}$$

$$B^2 = R_c^2(\varphi_{tr}) + \rho \left(R_c^2(\varphi_P) - R_c^2(\varphi_{tr}) \right), \tag{A 6}$$

$$B^3 = R_c^3(\varphi_{tr}) + \rho \left((R_c^3(\varphi_P) - R_c^3(\varphi_{tr}) \right). \tag{A 7}$$

For all points P in the ζ_α-domain for which $\zeta_2 < \cos\varphi_{tr}$ (e.g. P_2 in figure 12*b*) choose

$$\varphi_P = \arccos\zeta_2, \tag{A 8}$$

$$\rho = \frac{\zeta_1}{(1-\zeta_2^2)^{1/2}}, \tag{A 9}$$

and define the spine origin $\boldsymbol{B}$ as

$$B^1 = \rho R_c^1(\varphi_P), \tag{A 10}$$

$$B^2 = R_c^2(\varphi_P), \tag{A 11}$$

$$B^3 = R_c^3(\varphi_P). \tag{A 12}$$

Appendix B. An integral relation for the meniscus curvature

A useful integral relation for the meniscus curvature can be derived by integrating the Euler–Lagrange equations, corresponding to (9),

$$\left(\frac{\partial A_m^{1/2}}{\partial R^i_{m,\alpha}}\right)_{,\alpha} = \kappa N^i_m A_m^{1/2}, \tag{B 1}$$

over the (ζ_1, ζ_2), domain and applying the divergence theorem to obtain

$$\oint \left(\frac{\partial A_m^{1/2}}{\partial R^i_{m,\alpha}}\right) n_\alpha \mathrm{d}\varphi = \iint \kappa N^i_m {A_m}^{1/2} \mathrm{d}\zeta_1 \mathrm{d}\zeta_2, \tag{B 2}$$

where $\boldsymbol{n} = [\sin(\varphi), \cos(\varphi)]^T$ is the normal vector on the boundary of the (ζ_1, ζ_2)-domain. Using elementary differential geometry, this equation can be transformed into

$$\oint \frac{\partial \boldsymbol{R}_c(\varphi)}{\partial \varphi} \times \boldsymbol{N}_m \left|\frac{\partial \boldsymbol{R}_c(\varphi)}{\partial \varphi}\right| \mathrm{d}\varphi = \iint \kappa \boldsymbol{N}_m A_m^{1/2} \mathrm{d}\zeta_1 \mathrm{d}\zeta_2. \tag{B 3}$$

This expression equates the force exerted by the pressure jump over the meniscus with the surface tension along the contact line, acting as a line force tangential to the interface and normal to the contact line. For menisci with rotational symmetries about the z-axis (such as those considered in this study), only the z-component of this equation is non-zero and provides the following expression for κ:

$$\kappa = \frac{1}{\mathscr{A}_{proj}} \oint \frac{\partial \boldsymbol{R}_c(\varphi)}{\partial \varphi} \times \boldsymbol{N}_m \left|\frac{\partial \boldsymbol{R}_c(\varphi)}{\partial \varphi}\right| \mathrm{d}\varphi, \tag{B 4}$$

where $\mathscr{A}_{proj}$ is the area contained in the projection of the contact line onto the (x, y)-plane. For a given contact line position and wall shape, the normal vector on the meniscus, $\boldsymbol{N}_m$, is determined by the contact angle. Hence the entire right-hand side of the equation can be evaluated. In the numerical computations equation (B 4) was used as a further consistency check for the numerical results. Typically, κ predicted by (B 4) agreed with the computed value within a relative error of 10^{-4} and an increase beyond this value was usually a sign of insufficient spatial resolution.

For uniformly collapsed tubes, $\mathscr{A}_{proj}$ is equal to the tubes' cross-sectional area, $\mathscr{A}_{proj} = \mathscr{A}_{sect}$, and equation (B 4) can be further simplified to

$$\kappa = \frac{\mathscr{S} \cos\gamma}{\mathscr{A}_{sect}}, \tag{B 5}$$

where $\mathscr{S}$ is the arclength of the projection of the contact line onto the (x, y)-plane, which is equal to the tube's inner circumference. Equation (B 5) has frequently been used in the analysis of menisci in cylindrical tubes (see e.g. Finn 1986) and helped to explain the development of the meniscus finger in § 4.1.

Appendix C. The case $\gamma = 0$

This Appendix shows why the determination of the meniscus shape for zero contact angle ($\gamma = 0$) cannot be dealt with directly by the energy-based approach used in this study. We used the variational principle (9) to determine the meniscus shape for a given wall shape by minimizing the surface energy of the air–liquid interface, subject to the contact angle boundary condition. An alternative (but mathematically equivalent) formulation is given by the minimization of *all* surface energies (i.e.

including the wall–fluid surface energies). The corresponding form of the variational principle (9) is given by

$$\int\!\!\int \left(\delta \mathscr{A}_m^{1/2} - \kappa\, \boldsymbol{N}_m \cdot \delta \boldsymbol{R}_m \mathscr{A}_m^{1/2}\right) \mathrm{d}\zeta_1\, \mathrm{d}\zeta_2 - \beta\, \delta \int\!\!\int \mathscr{A}_w^{1/2}\, \mathrm{d}\xi_1\, \mathrm{d}\xi_2 = 0, \qquad \text{(C 1)}$$

where $\beta = (\sigma_{wa} - \sigma_{wl})/\sigma$ is the spreading coefficient which is related to the contact angle by $\beta = \cos\gamma$, because of Young's equation (10). $\mathscr{A}_w = |\boldsymbol{R}_{w,1} \times \boldsymbol{R}_{w,2}|^2$ is the determinant of the metric tensor of the inner wall surface parametrized by (ξ_1, ξ_2). The last integral in (C 1) describes the change in the total wall–fluid surface energy (given by the sum of the wall–liquid and wall–air surface energies, which are the products of the wetted and dry wall surface areas with the respective surface tensions) during a virtual displacement of the contact line. Carrying out the variations of the second integral generates Young's equation (10) as an essential boundary condition for the unchanged Euler–Lagrange equations (B 1).

For zero contact angle the meniscus meets the tube wall tangentially and we have $\beta = 1$ and therefore $\sigma_{wa} - \sigma_{wl} = \sigma$. During a variation of the contact line position, the decrease in wetted wall area is equal to the increase in dry wall area. Hence it is always possible to extend any given meniscus shape by advancing the contact line into the previously dry wall area and generating a 'wet collar' between the old and new contact line positions without changing the overall energy balance: The increase in the air–liquid surface energy is exactly compensated by the decrease in the total wall–fluid surface energy (note that $\boldsymbol{N}_m \cdot \delta \boldsymbol{R}_m = 0$ on the 'wet collar'). This causes the energy minimization to fail and as one approaches the limit $\gamma \to 0$ in the computations, the convergence of the Newton iteration becomes increasingly slow. At the same time the contact line becomes increasingly wavy since its position becomes less constrained by the energy minimization. For $\gamma = 0$, the Newton iteration fails to converge.

REFERENCES

Bailey, A. I. 1961 Friction and adhesion of clean and contaminated mica surfaces. *J. Appl. Phys.* **32**, 1407–1412.

Bailey, A. I. & Kay, S. M. 1967 A direct measurement of the influence of vapour, of liquid and of oriented monolayers on the interfacial energy of mica. *Proc. R. Soc. Lond.* A **301**, 47–56.

Batchelor, G. K. 1967 *An Introduction to Fluid Dynamics.* Cambridge University Press.

Becker, E. B., Carey, G. F. & Oden, J. T. 1984 *Finite Elements: An Introduction.* Prentice-Hall.

Bogner, F. K., Fox, R. L. & Schmit, L. A. 1967 A cylindrical shell discrete element. *AIAA J.* **5**, 745–750.

Carmo, M. P. do 1976 *Differential Geometry of Curves and Surfaces.* Prentice-Hall.

Carré, A., Gastel, J.-C. & Shanahan, M. E. R. 1996 Viscoelastic effects in the spreading of liquids. *Nature* **379**, 432–434.

Concus, P. & Finn, R. 1974 On capillary surfaces in the absence of gravity. *Acta Mathematica* **132**, 177–198.

Everett, D. H. & Haynes, J. M. 1972 Model studies of capillary condensation. *J. Colloid Interface Sci.* **38**, 125–137.

Extrand, C. W. & Kumagai, Y. 1996 Contact angles and hysteresis on soft surfaces. *J. Colloid Interface Sci.* **184**, 191–200.

Finn, R. 1986 *Equilibrium Capillary Surfaces.* Grundlehren der Mathematischen Wissenschaften, vol. 284. Springer.

Fortes, M. A. 1984 Deformation of solid surfaces due to capillary forces. *J. Colloid Interface Sci.* **100**, 17–26.

Gauglitz, P. A. & Radke, C. J. 1988 An extended evolution equation for liquid film breakup in cylindrical capillaries. *Chem. Engng Sci.* **43**, 1457–1465.

Gaver, D. P. III, Samsel, R. W. & Solway, J. 1990 Effects of surface tension and viscosity on airway reopening. *J. Appl. Physiol.* **69**, 74–85.

Gibbs, J. W. 1906 *The Scientific Papers of J. Willard Gibbs.* Longmans, Green.

Goren, S. L. 1962 The instability of an annular thread of fluid. *J. Fluid Mech.* **12**, 309–319.

Grotberg, J. B. 1994 Pulmonary flow and transport phenomena. *Ann. Rev. Fluid Mech.* **26**, 529–571.

Halpern, D. & Grotberg, J. B. 1992 Fluid-elastic instabilities of liquid-lined flexible tubes. *J. Fluid Mech.* **244**, 615–632.

Halpern, D. & Grotberg, J. B. 1993 Surfactant effects on fluid-elastic instabilities of liquid-lined flexible tubes: a model of airway closure. *Trans. ASME : J. Biomech. Engng* **115**, 271–277.

Hammond, P. S. 1983 Nonlinear adjustment of a thin annular film of viscous fluid surrounding a thread of another within a circular cylindrical pipe. *J. Fluid Mech.* **137**, 363–384.

Heil, M. 1996 The stability of cylindrical shells conveying viscous flow. *J. Fluids Struct.* **10**, 173–196.

Heil, M. 1997 Stokes flow in a collapsible tube – computation and experiment. *J. Fluid Mech.* **353**, 285–312.

Heil, M. 1998 Stokes flow in an elastic tube – a large-displacement fluid-structure interaction problem. *Intl J. Numer. Meth. Fluids* **28**, 243–265.

Heil, M. & Pedley, T. J. 1996 Large post-buckling deformations of cylindrical shells conveying viscous flow. *J. Fluids Struct.* **10**, 565–599.

Jensen, O. E. 1997 The thin liquid lining of a weakly curved cylindrical tube. *J. Fluid Mech.* **331**, 373–403.

Johnson, M., Kamm, R. D., Ho, L. W., Shapiro, A. & Pedley, T. J. 1991 The nonlinear growth of surface-tension-driven instabilities of a thin annular film. *J. Fluid Mech.* **233**, 141–156.

Kamm, R. D. & Schroter, R. C. 1989 Is airway closure caused by a liquid film instability? *Respir. Physiol.* **75**, 141–156.

Kirstein, A. F. & Wenk, E. 1956 Observations of snap-through in action in thin cylindrical shells under external pressure. *Soc. Exptl Stress Analysis Proc.* **XIV**, 205–214.

Kistler, S. F. & Scriven, L. E. 1983 Coating flows. In *Computational Analysis of Polymer Processing* (ed. J. R. A. Pearson & S. M. Richardson). Applied Science Publishers, London.

Landau, L. D. & Lifshitz, E. M. 1987 *Fluid Mechanics.* Pergamon.

Long, D., Ajdari, A. & Leibler, L. 1996 Static and dynamic wetting properties of thin rubber films. *Langmuir* **12**, 5221–5230.

Maddocks, J. H. 1987 Stability and folds. *Arch. Rat. Mech. Anal.* **99**, 301–328.

Macklem, P. T., Proctor, D. F. & Hogg, J. C. 1970 The stability of the peripheral airways. *Respir. Physiol.* **8**, 191–203.

Michael, D. H. 1981 Meniscus stability. *Ann. Rev. Fluid Mech.* **13**, 189–215.

Otis, D. R., Petak, F., Hantos, Z., Fredberg, J. J. & Kamm, R. D. 1996 Airway closure and reopening assessed by the alveolar capsule oscillation technique. *J. Appl. Physiol.* **80**, 2077–2084.

Pethica, B. A. 1977 The contact angle equilibrium. *J. Colloid Interface Sci.* **62**, 567–569.

Rast, M. P. 1994 Simultaneous solution of the Navier-Stokes and elastic membrane equations by a finite element method. *Intl J. Numer. Meth. Fluids* **19**, 1115–1135.

Shanahan, M. E. R. 1985 Contact angle equilibrium on thin elastic solids. *J. Adhesion* **18**, 247–267.

Simitses, G. J. 1976 *An Introduction to the Elastic Stability of Structures.* Prentice Hall.

Struwe, M. 1988 *Plateau's Problem and the Calculus of Variations.* Mathematical Notes 35. Princeton University Press.

Thompson, J. M. T. & Hunt, G. W. 1973 *A General Theory of Elastic Stability.* John Wiley & Sons.

Wempner, G. 1973 *Mechanics of Solids.* McGraw-Hill.

West, J. B. 1995 *Respiratory Physiology – the Essentials*, 5th edn. Williams & Wilkins, Baltimore.

Yamaki, N. 1984 *Elastic Stability of Circular Cylindrical Shells.* North-Holland.

Yap, D. Y. K., Liebkemann, W. D., Solway, J. & Gaver, D. P. 1994 The influence of parenchymal tethering on the reopening of closed pulmonary airways. *J. Appl. Physiol.* **76**, 2095–2105.